Chemical Geology 674 (2025) 122578

Contents lists available at ScienceDirect

Chemical Geology

journal homepage: www.elsevier.com/locate/chemgeo

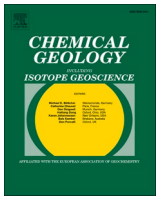

Fluid evolution and halogen fractionation in orogenic belts: A comparative fluid inclusion appraisal in the Eastern Pyrenees

Eloi González-Esvertit [a,b,c,*], Tobias Fusswinkel [d], Àngels Canals [a], Josep Maria Casas [e], Joyce Neilson [f], Thomas Wagner [d], Enrique Gomez-Rivas [a]

[a] Departament de Mineralogia, Petrologia i Geologia Aplicada, Facultat de Ciències de la Terra, Universitat de Barcelona, 08028 Barcelona, Spain
[b] Geosciences Barcelona (GEO3BCN-CSIC), C/ Lluís Solé i Sabarís s/n, 08028 Barcelona, Spain
[c] Institut de Recerca Geomodels, Universitat de Barcelona, 08028 Barcelona, Spain
[d] Institute of Applied Mineralogy and Economic Geology, RWTH Aachen University, 52062 Aachen, Germany
[e] Departament de Dinàmica de la Terra i l'Oceà, Facultat de Ciències de la Terra, Universitat de Barcelona, 08028 Barcelona, Spain
[f] School of Geosciences, King's College, University of Aberdeen, AB24 3UE Aberdeen, United Kingdom

ARTICLE INFO

Editor: Marco Fiorentini

Keywords:
Fluid Inclusions
LA-ICP-MS
Triple-halogen microanalysis
Fluid-rock interaction
Halogen fractionation
Fluid evolution
Pyrenees

ABSTRACT

The physicochemical signatures of fluid-rock interaction, recorded in fluid inclusions, represent fundamental proxies for understanding the interplay between rock deformation, fluid migration, and ore deposit formation in the Earth's crust. Although fluid-rock interaction can take place simultaneously or sequentially both in the basement and the cover of collisional orogens, these two scenarios are generally investigated separately, thus precluding an integrated understanding of the processes involved. Here, we present a comprehensive study of the fluid evolution in the basement and cover rocks of the Pyrenees (SW Europe) by means of Geographic Information System (GIS)-assisted petrography, microthermometry, Electron Backscatter Diffraction (EBSD), Raman micro-spectroscopy, and Laser Ablation Inductively Coupled Plasma Mass Spectrometry (LA-ICP-MS) microanalysis of individual fluid inclusions. The investigated fluids are sampled from giant quartz veins, which are tens of meters wide and up to several kilometres long. Two-phase aqueous fluid inclusions hosted in the basement (Canigó and Cap de Creus massifs) and cover rocks (Roc de Frausa massif) show significant variations regarding their homogenization temperature (T_h), salinity, and chemical composition. Basement-hosted H_2O-NaCl-$CaCl_2$ fluids have T_h and salinity ranging between 190 and 220 °C and 12–16 wt% equivalent (eq.) NaCl in the Canigó massif, and between 190 and 260 °C and 16–20 wt% eq. NaCl in the Cap de Creus massif. Conversely, T_h of 180–240 °C and salinity of 4–7 wt% eq. NaCl were obtained for H_2O-NaCl cover rock-hosted fluids in the Roc de Frausa massif. Fluid salinity, cation concentrations, and halogen ratios suggest that basement-hosted fluids represent residual basinal brines that originated from seawater which underwent variable degrees of evaporation and organic matter interaction. In contrast, cover rock-hosted fluids represent seawater-like precursor fluids that record strong organic matter interaction without significant evaporative halogen fractionation. The data suggest that neither basement- nor cover-hosted fluids were released at depth from magmatic or metamorphic fluids, which agrees with geological constraints of the investigated areas. However, fluids from both basement and cover rocks infiltrated deep into the subsurface, as revealed by their variable metal and halogen concentration suggesting compositionally stratified fluid compositions at depth. Our data and conclusions differ from fluid inclusion studies reported for other giant quartz vein systems worldwide, suggesting that different fluid origins and evolution histories may drive the formation of these large quartz accumulations. Moreover, the large variations of the Br/Cl, I/Cl, and Br/I ratios show that halogen ratios should be used with caution: they are excellent tracers of the fluid evolution history, but may not provide a straightforward fluid origin classification.

* Corresponding author at: Departament de Mineralogia, Petrologia i Geologia Aplicada, Facultat de Ciències de la Terra, Universitat de Barcelona, 08028 Barcelona, Spain.
E-mail address: e.gonzalez-esvertit@ub.edu (E. González-Esvertit).

https://doi.org/10.1016/j.chemgeo.2024.122578
Received 20 July 2024; Received in revised form 2 December 2024; Accepted 14 December 2024
Available online 18 December 2024

1. Introduction

Understanding the origin of geological fluids, and the mechanisms driving their flow and evolution through space and time, is crucial for determining the processes involved before, during, and after the formation of collisional mountain belts (e.g., Koons and Craw, 1991; Mullis et al., 1994; Yardley, 1997; Goldfarb et al., 2001; MacKenzie et al., 2008; Goldfarb and Groves, 2015). Orogens are favourable environments for the coexistence of fluids originating from various sources, because orogenesis often involves coexisting magmatism, regional metamorphism, and the development and progressive deformation of foreland and intramontane sedimentary basins (Bonin, 1990; Brown, 1995; DeCelles and Giles, 1996). From the fluid infiltration down to significant depths, or from fluid release via metamorphic devolatilization reactions or magma reservoirs at depth, marine, meteoric, metamorphic, and magmatic fluids (and their mixing products) may interact with subsurface rocks as they migrate (e.g., Yardley, 2005; Wagner et al., 2010). During these fluid-rock interaction processes, fluids and rocks react chemically and exchange major and trace elements. This causes mineralogical changes in the rocks and results in essentially rock-buffered fluid compositions (e.g., Marsala et al., 2013; Miron et al., 2013; Marsala and Wagner, 2016; Rauchenstein-Martinek et al., 2016) depending on the type of rock (or melt) that has hosted the fluid, sometimes overprinting the compositional features that are diagnostic of the fluids source (e.g., Kendrick et al., 2001; Yardley, 2005; Pettke et al., 2012; Fusswinkel et al., 2018). The most direct samples (often the only ones accessible) of the fluids that have circulated at some stage in the geological evolution of rocks are fluid inclusions (e.g., Sorby, 1858; Roedder, 1984; Goldstein and Reynolds, 1994). Therefore, establishing the temperature, pressure, and composition of the fluids trapped in such inclusions may reveal not only the fluid sources but also the rocks with which fluids have interacted along their migration pathways, providing valuable insights into the crustal element fluxes, the dynamics of stress redistribution at seismogenic depths, and the formation mechanisms of ore deposits, among other aspects (e.g., Ridley and Diamond, 2000; Cox, 2005; Bons et al., 2014).

Although fluids derived from different sources coexist in orogenic settings, their evolution is often investigated separately in two distinct environments, the basement (e.g., Cardellach et al., 1992; Pettke et al., 2010; Tang et al., 2021; Yang et al., 2022; Bongiovanni et al., 2024) and the cover (e.g., Banks et al., 1991; Vandeginste et al., 2012). Therefore, even if mixing between fluids from different sources is recognized in fluid inclusions from a given area (Klemm et al., 2004; Fusswinkel et al., 2013; Walter et al., 2018), there is a lack of integrative approaches addressing the evolution of fluids that simultaneously or sequentially interact with, and lie within, the basement and the cover rocks of orogenic belts (Gleeson et al., 2000; Cathelineau et al., 2012). Moreover, interpretations on fluid mixing that infer both downward and upward fluid-flow trajectories converging at the mixing site have been suggested to be hydrodynamically unrealistic scenarios, since they would imply a concentric hydraulic head field and a fluid sink at the (central) zone of lowest hydraulic potential (Bons et al., 2012, 2014; de Riese et al., 2020).

Combined microthermometry, Raman micro-spectroscopy, and Laser Ablation Inductively Coupled Plasma Mass Spectrometry (LA-ICP-MS) microanalysis of individual fluid inclusions is increasingly recognized as a robust approach to elucidate fluid sources and fluid evolution (Audétat et al., 2008; Pettke et al., 2012; Bons et al., 2014; Wagner et al., 2016; Bons and Gomez-Rivas, 2020; Scharrer et al., 2021; Fusswinkel et al., 2022). In contrast to analysis of fluids extracted from bulk samples (e.g., crush-leach ion chromatography or solution ICP-MS), which may result in averaged compositions and mixed concentration estimates when different fluid types exist in a sample, in-situ LA-ICP-MS analysis allows consideration of petrographic constraints on fluid composition (Heinrich et al., 2003; Wilkinson, 2014; Wagner et al., 2016). Therefore, the elemental concentrations of groups of fluid inclusions that were trapped at the same time (i.e., Fluid Inclusion Assemblages; FIAs; Goldstein and Reynolds, 1994) can be differentiated in a sample by obtaining single-inclusion compositions and then averaging the results using only textural constraints. Recent analytical advances have, furthermore, allowed the quantification of triple halogen compositions (Cl, Br, and I) in fluid inclusions (Fusswinkel et al., 2018). Since fractionation of these halogens during fluid-rock interaction is generally limited, processes such as evaporation, evaporite dissolution, and organic matter interaction commonly result in characteristic Cl, Br, and I signatures of crustal fluids even in cases where they migrate along protracted flow paths. Accordingly, halogen ratios are excellent fluid provenance tracers (Fu et al., 2012; Kendrick, 2018; Pirajno, 2018), and their quantification through LA-ICP-MS is very useful for comparative appraisals of the fluid sources and their evolution in the basement and cover rocks of collisional belts (Fusswinkel et al., 2018, 2022; Scharrer et al., 2023).

The Pyrenees (Fig. 1) represents an outstanding natural laboratory for the study of fluid evolution in orogenic belts due to the excellent outcrop conditions and the well-known structural and stratigraphical evolution of its basement and cover rocks (Burbank et al., 1992; Muñoz, 1992; Casas et al., 2010; Ford and Vergés, 2021; Liesa et al., 2021; Cruset et al., 2023; González-Esvertit et al., 2025). Insight into cover rock fluid evolution in the southern Pyrenees has been obtained through $\delta^{13}C$, $\delta^{18}O$, $^{87}Sr/^{86}Sr$ analyses and clumped isotope thermometry on calcite cements (Lacroix et al., 2018; Nardini et al., 2019; Muñoz-López et al., 2022). Fluids in the basement rocks of the Axial zone have been studied through fluid inclusion microthermometry and crush-leach analysis (Ayora and Casas, 1983; McCaig et al., 1990; Banks et al., 1991; McCaig et al., 2000; González-Esvertit et al., 2020). Therefore, the fluid inclusion compositions in this region have only been evaluated for the basement rocks and these studies were restricted to analytical techniques that lack the space-time resolution of LA-ICP-MS microanalysis. There is, therefore, a missing link between fluid evolution histories recorded in both the cover and the basement rocks of the Pyrenees, although mixing processes between surface-derived and deep-sourced fluids are present in this region (Wickham and Taylor, 1987; McCaig et al., 2000; Lacroix et al., 2014).

Here we present the results of a comparative fluid inclusion study across the Eastern Pyrenees (Fig. 1). Research has been carried out in quartz samples from veins up to tens of metres wide and several kilometres long (i.e., Giant Quartz Veins; GQVs), which are hosted both in the basement and cover rocks of the orogen (hereafter “orogenic settings”) and are evidence for large-scale paleofluid flow systems. Recently, these structures have been interpreted as products of fluid-driven Si-metasomatism where the original fabrics and features of precursor rocks were overprinted during coupled deformation and fluid migration (e.g., González-Esvertit et al., 2024). The overreaching aim of this work is to elucidate the differences and similarities of the sources and evolution history of fluids within the basement and the cover rocks of the Pyrenees, and whether or not the fluid properties varied as a function of trapping depth. Moreover, we assess if the concentrations of halogens, base metals and other cation ratios may unravel distinct host rock lithologies involved in fluid-rock interaction. Texturally constrained elemental analysis through LA-ICP-MS (including halogens) of individual fluid inclusions, coupled with fluid temperature, and salinity determinations, allow assessment and comparison of sources and evolution of fluids in three different sectors (hereafter “study areas”) representing both basement (Canigó and Cap de Creus areas) and cover (Roc de Frausa area) orogenic settings. Essential fluid inclusion petrography is recorded through a novel Geographic Information System (GIS)-based thin section mapping workflow that facilitates subsequent analytical work and data quality assessment. The reliability of fluid inclusion data is further evaluated using Electron Backscatter Diffraction (EBSD) as a pilot test, since this method may allow the identification of crystal zones with low or high intracrystalline deformation and thus reveal the reliability of different FIAs. The results of this

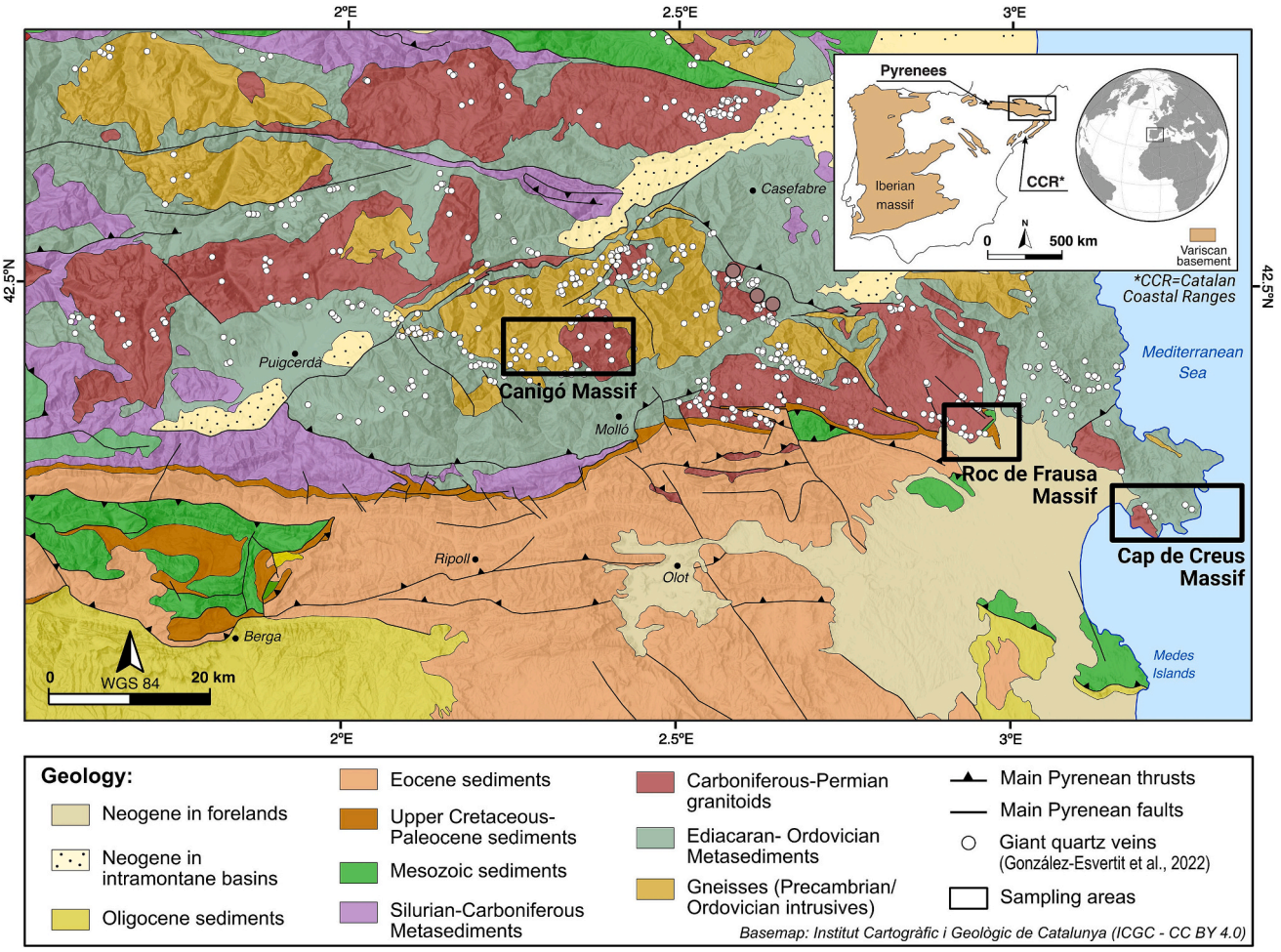

Fig. 1. Geological sketch map of the Central-Eastern Pyrenees showing the spatial distribution of giant quartz veins within the basement and the cover rocks, as well as the location of the study areas.

study contribute to understanding the physicochemical signatures of fluid-rock interaction during fluid flow, rock deformation, and ore deposit formation, along with the fluid evolution history at the Iberian-Eurasian plate boundary.

2. Geological setting

The Pyrenees is an asymmetric, doubly verging, E-W trending Alpine fold-and-thrust belt that formed from the Late Cretaceous to Miocene after the collision between the Iberian and Eurasian plates (e.g., Muñoz, 1992; Vergés et al., 2019). The Alpine deformation resulted in the formation of a central antiformal stack with three main thrust sheets, which exhumed pre-Alpine basement rocks: late Neoproterozoic–to–Carboniferous metasediments, Variscan orthogneisses derived from late Neoproterozoic and Ordovician intrusives, and late-Variscan granitoids (Fig. 1). These rocks record Cadomian, Ordovician and Variscan magmatism, Sardic (Ordovician), Variscan and Alpine deformation phases, and a Variscan regional metamorphism (Santanach, 1972; Muñoz, 1992; Casas, 2010; Navidad et al., 2018; Padel et al., 2018; Liesa et al., 2021). Thrust sheets forming the central antiformal stack are part of the southern orogenic wedge (Muñoz, 1992), and comprise Mesozoic evaporite and carbonate successions and mostly detrital Cenozoic rocks (Puigdefàbregas et al., 1992; Muñoz et al., 2013; Muñoz et al., 2018; González-Esvertit et al., 2023).

Investigations on fluid flow and fluid evolution in the Pyrenees have been mostly focused on mineral veins, cements, and hydrothermal dolomitization occurring within the cover orogenic setting of the southern and northern parts of the chain (e.g., Canals et al., 1999; Travé et al., 2007; Lacroix et al., 2014; Quesnel et al., 2019; Sun et al., 2022). By contrast, few investigations within the basement rocks (Fig. 1) are focused on high-temperature magmatic and metamorphic fluids related to skarn mineralization (e.g., Cardellach et al., 1992; Delgado and Soler, 2010), as well as on fluid migration along Variscan and Alpine faults (McCaig et al., 1990; McCaig et al., 2000; Muñoz-López et al., 2020).

Hundreds of quartz veins up to tens of metres wide and up to several kilometres long (i.e., Giant Quartz Veins; GQVs) are hosted in rocks of different ages and composition in the Pyrenees (González-Esvertit et al., 2022a). Most of these structures crop out along the Axial Zone (Figs. 2, 3), although some of them also occur in the cover rocks of the North Pyrenean and South Pyrenean areas (Figs. 1, 4; González-Esvertit et al., 2022b). The age of these structures is under discussion. They have classically been attributed to the Variscan Orogeny, i.e., postdating the late-Variscan magmatic rocks where they are hosted (Figs. 1–3), although a post-Variscan age may be inferred from the age of other Mesozoic host rocks (Fig. 4).

The GQVs of the Pyrenees (Fig. 5a-c) show two main quartz growth stages independently of their location and host rock types (Ayora and Casas, 1983; Ayora et al., 1984; Casas, 1984; González-Esvertit et al., 2022b; González-Esvertit et al., 2022a). The first stage occurs as a deformed quartz mass that makes up most of the exposed areas of the GQVs (Type-1 quartz) (Fig. 5d). It records protocataclastic to ultramylonitic deformation and is associated to symmetric silicification haloes with replacement textures affecting the adjacent host rocks. The second quartz growth stage (Type-2 quartz) is characterized by euhedral

quartz crystals that are present in cavities postdating the main GQV (Fig. 5e-g). The study of Ayora and Casas (1983) is the only one that focused on the fluid evolution recorded within these GQVs, where quartz-hosted fluid inclusions from the Canigó massif (Fig. 3) are characterized by microthermometry and crush-leach dissolved solutes extraction and absorption spectroscopy analysis. Here we provide a comparative fluid inclusion appraisal of GQV quartz from basement and cover orogenic settings (Figs. 2–4). Accordingly, geological summaries of the study areas are provided below.

2.1. Geological setting of basement-hosted fluids

Fluid evolution within the basement rocks of the Pyrenees is investigated in the Cap de Creus (Figs. 1, 2, 5b) and Canigó (Figs. 1, 3, 5a) massifs. The Cap de Creus massif study area (Figs. 1, 2) exposes a late Neoproterozoic-early Cambrian siliciclastic metasedimentary sequence of metagreywackes and biotite schists (± cordierite and sillimanite). They record a Variscan low-pressure high-temperature metamorphism, with a metmaorphic grade increasing nowadays towards the NW, from greenschist facies up to migmatite occurrence (Druguet, 1997; Carreras, 2001; Castiñeiras et al., 2008). Successive deformation episodes are registered by fold superposition, three cleavage generations, and regional-scale ductile shear zones that crosscut the rest of the Variscan macrostructure (Druguet, 1997; Llorens et al., 2013; Vissers et al., 2017; Druguet and Carreras, 2019). The investigated GQV in the Cap de Creus massif postdates the three main cleavages, the biotite and hornblende Roses granodiorite (290.8 ± 2.9 Ma; Druguet et al., 2014), and its contact metamorphic aureole (González-Esvertit et al., 2022b). The GQV (Figs. 2, 5b, e) is defined by several NW-SE-trending aligned discontinuous quartz bodies, which are sometimes affected by NW-SE-oriented mylonitic bands (González-Esvertit et al., 2022b; Fig. 2).

The Canigó massif study area (Figs. 1, 3) is a W-E-trending antiformal structure. It exposes a 3000 m-thick package of Variscan granitic orthogneisses (Guitard, 1965, 1970; Casas, 1984) derived from

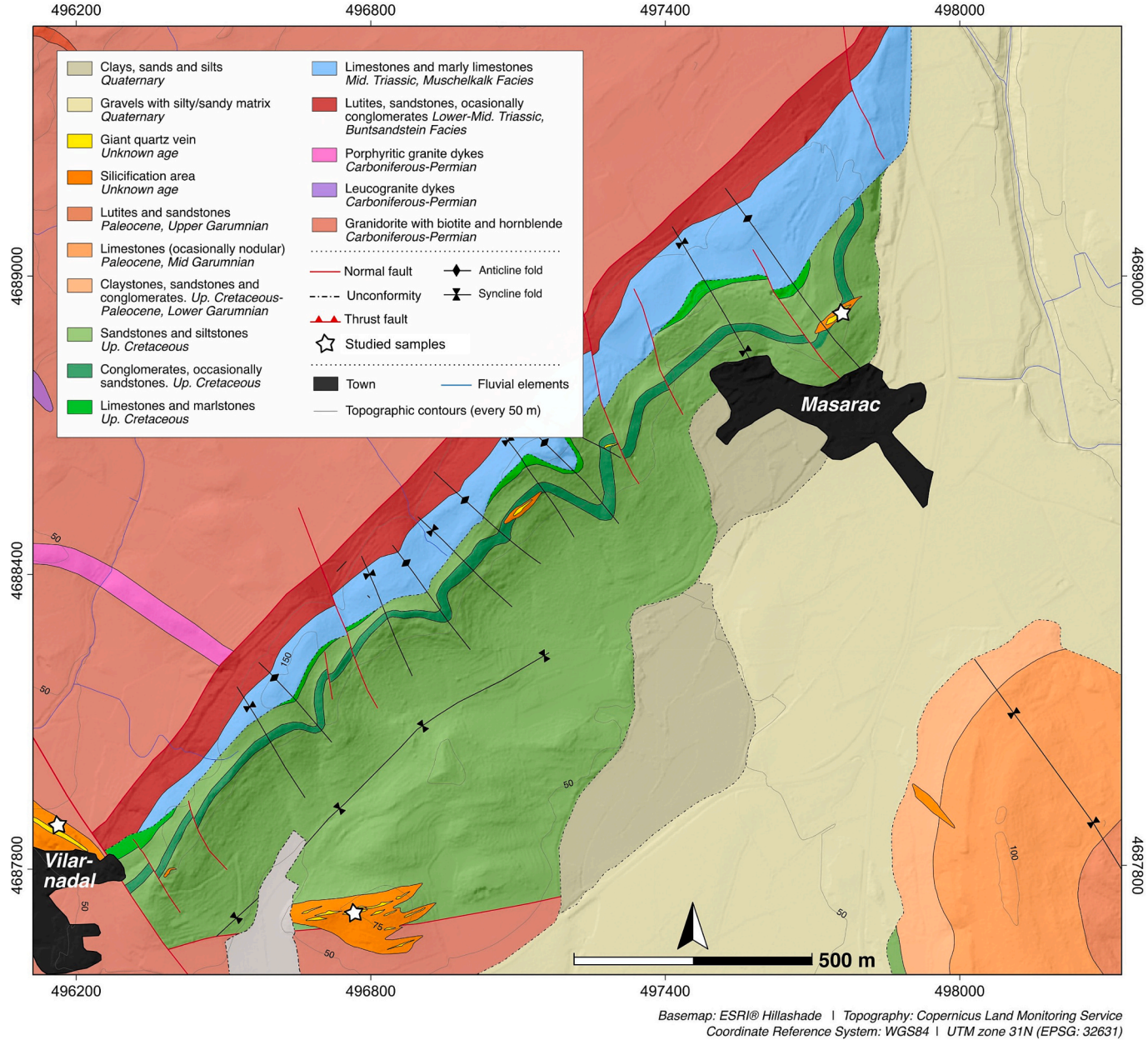

Fig. 4. Simplified geological map of the study area for cover-hosted fluids in the southern slope of the Roc de Frausa massif, with the location of the studied samples (see detailed version with structural data in González-Esvertit et al., 2022b).

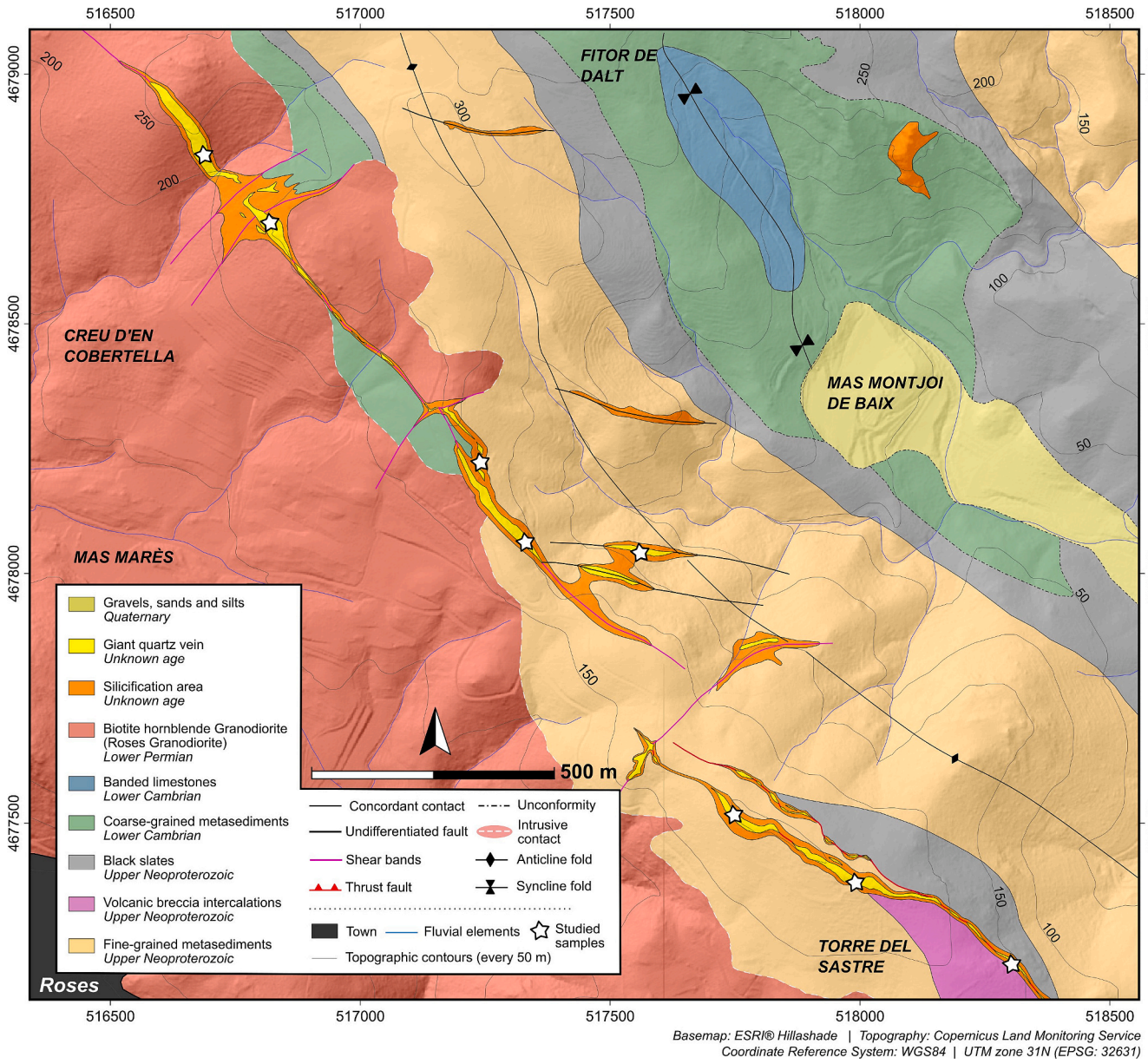

Fig. 2. Simplified geological map of the study area for basement-hosted fluids in the Cap de Creus massif, with the location of the studied samples (see detailed version with structural data in González-Esvertit et al., 2022b).

Ordovician intrusives (457–464 ± 2 Ma; Navidad et al., 2018) intercalated in a ca. 4000 m-thick pre-Upper Ordovician metasedimentary sequence (Laumonier et al., 2015; Casas et al., 2010; Padel et al., 2018). In the core of the massif, a late-Variscan peraluminous biotite-bearing monzogranite (285.4 ± 2.2 Ma and 302 ± 4 Ma; Laumonier et al., 2015) postdates the polyphase Variscan deformation and regional metamorphism (Guitard, 1970; Casas, 1984). GQVs in the Canigó massif (Figs. 3, 5a, d, f) crop out as discontinuous quartz bodies of tens of meters wide and hundreds to thousands of meters long that postdate all the aforementioned rock units (Casas, 1984; Laumonier et al., 2015). The Type-1 GQV quartz records a heterogeneously-developed E-W-trending mylonitic foliation.

2.2. Geological setting of cover-hosted fluids

Fluid evolution within the cover rocks of the Pyrenees is investigated in the southern slope of the Roc de Frausa massif (Fig. 4). This study area is located at the southeasternmost limit of a Variscan E-W-oriented biotite and hornblende rich granodiorite (311 ± 1; Aguilar et al., 2014) that is crosscut by leucogranite and granite porphyry dykes (Liesa, 1988; Vilà et al., 2005; Liesa et al., 2021). Three main synform-shaped Alpine structures formed by Mesozoic and Cenozoic sedimentary rocks unconformably overlie this granodiorite (Cirés et al., 1994; González-Esvertit et al., 2022b). The sedimentary sequence within the Vilarnadal-Masarac SW-NE-oriented syncline consists of claystones and sandstones of the Lower Triassic Buntsandstein facies, and laminated limestones, marly limestones, and minor dolostones of the Mid Triassic lower Muschelkalk facies. Triassic rocks are unconformably overlain by Upper Cretaceous sandstones and siltstones with minor intercalations of limestones, marlstones, and conglomerates. Mesozoic-Cenozoic rocks (upper Cretaceous-Palaeocene Garumnian facies) are formed by claystones, greyish limestones, and sandstone intercalations. All these rocks exhibit an Alpine fold interference pattern; a major SW-NE-oriented syncline that is further folded by minor NW-SE-oriented anticline-syncline pairs. GQVs in this area (Fig. 5c, g) are hosted in the granodiorite and in the Upper Cretaceous sedimentary rocks, following

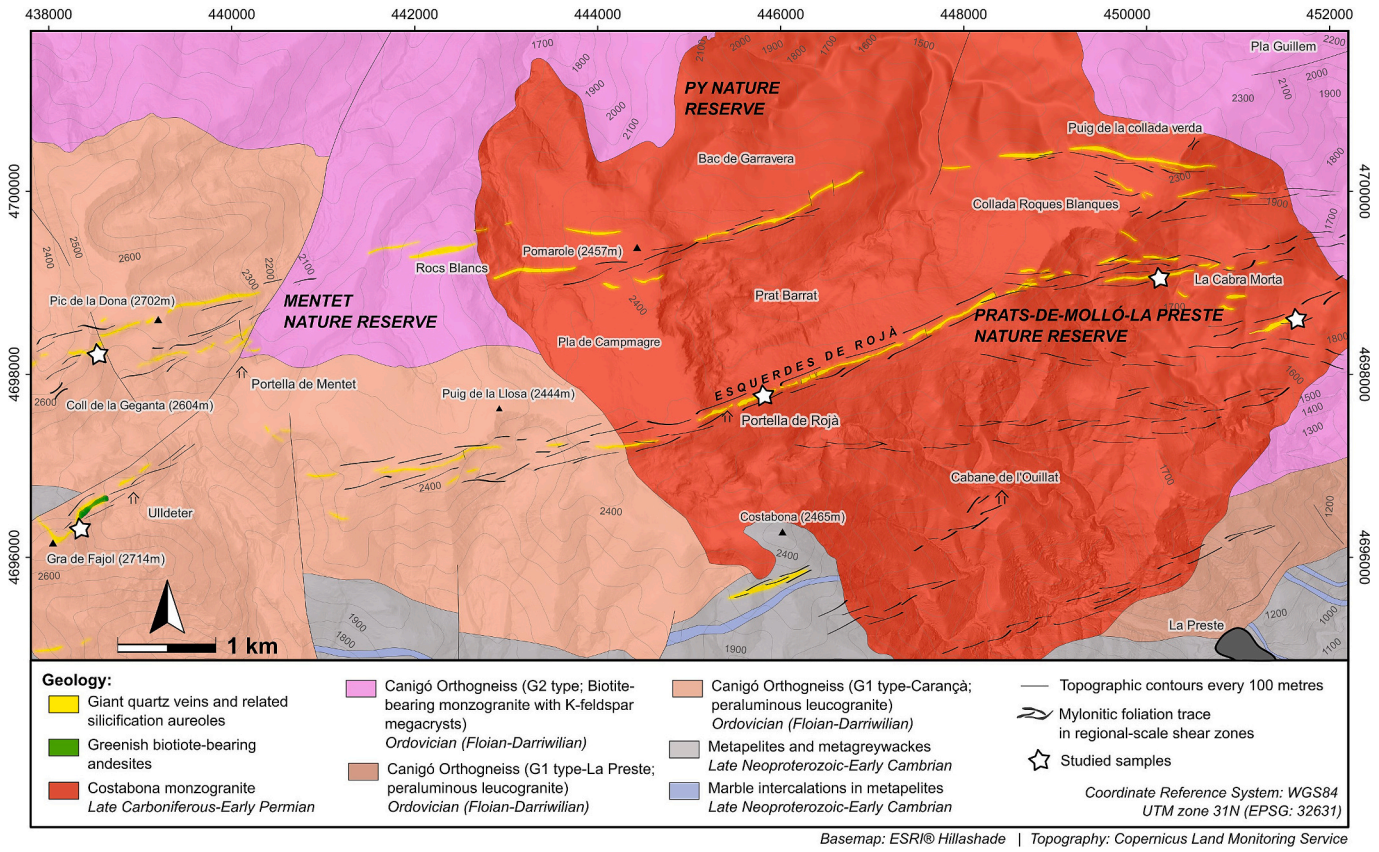

Fig. 3. Simplified geological map of the study area for basement-hosted fluids in the Canigó massif, with the location of the studied samples.

the main trend of a conglomerate level. They generally follow the fold limbs of the major SW-NE-oriented syncline (Fig. 4) and show incipient mylonitic foliation in the Type-1 quartz.

3. Materials and methods

3.1. Sampling

Type-1 (deformed; Fig. 5d) and Type-2 (euhedral; Fig. 5e-g) quartz crystals found within GQVs were sampled at 36 localities from the Cap de Creus (Fig. 2), Canigó (Fig. 3), and Roc de Frausa (Fig. 4) areas in the Eastern Pyrenees. After careful hand-specimen description, 16 samples were selected for further petrographic and fluid inclusion characterization (Figs. 2–4). Doubly polished, 300 μm-thick sections were prepared for those samples containing well-exposed growth features to carry out the petrographic characterization of fluid inclusions. Standard 30 μm-thick sections from the same samples were also used to assess the quartz textures and microstructures using optical microscopy, Scanning Electron Microscopy (SEM), and EBSD. The most representative samples in terms of geographical distribution, host rock types, and fluid inclusion modes of occurrence were subsequently examined in detail. The metadata of the investigated samples are provided in the Supplementary Material 1 (SM1).

3.2. Electron Backscatter Diffraction (EBSD)

EBSD analyses were carried out at the ACEMAC Facility (University of Aberdeen) using a Nordlys Nano EBSD detector coupled to a Carl Zeiss GeminiSEM 300 High Resolution Field Emission SEM. Type-1 and Type-2 quartz crystals from the Canigó massif were selected for SEM-EBSD analyses on the basis of the occurrence or absence of deformation microstructures to evaluate and compare the reliability of fluid inclusion analyses. These were: (i) a deformed quartz sample with dynamically recrystallized areas through subgrain rotation recrystallization (Type-1) and (ii) a chiefly undeformed sample showing euhedral quartz crystals with growth bands containing primary fluid inclusions (Type-2). Polished carbon-coated thin sections of both samples were tilted 70° and scanned with the EBSD detector under high vacuum using an accelerating voltage of 20 kV, at working distances between 14 and 20 mm. Step size was set between 5 and 8 μm depending on sample grain size. EBSD pattern indexing and data curation processes were carried out using the AZtecHKL, AZtecOne, and AZtecCrystal software suites (Oxford Instruments®).

3.3. Fluid inclusion GIS-based petrography and microthermometry

Petrography of fluid inclusions was carried out using the Fluid Inclusion Assemblage (FIA) approach (Diamond, 1990; Goldstein and Reynolds, 1994; Goldstein, 2001). Accordingly, 50 FIAs were identified and classified as primary, pseudosecondary, and secondary assemblages according to their origin and relative timing relationships (e.g., Goldstein and Reynolds, 1994). Assuming homogeneous trapping and similar phase ratios were used as criteria for ensuring that the studied inclusions indeed belong to distinct FIAs (Roedder, 1984; Bodnar, 2003). Only FIAs showing a clear petrographic relationship with the growth of their host quartz crystal were classified as primary. The petrographic features of each FIA are provided in the SM1.

Individual fluid inclusions belonging to FIAs were mapped following a GIS-based approach. High-resolution thin section scans were obtained using a commercial film scanner and subsequently imported into a GIS environment. Thin section scans were used as a base map where either focus-stacked or standard microphotographs taken at increasing magnifications were manually georeferenced. The superposed thin section scans and microphotographs from each investigated thin section were

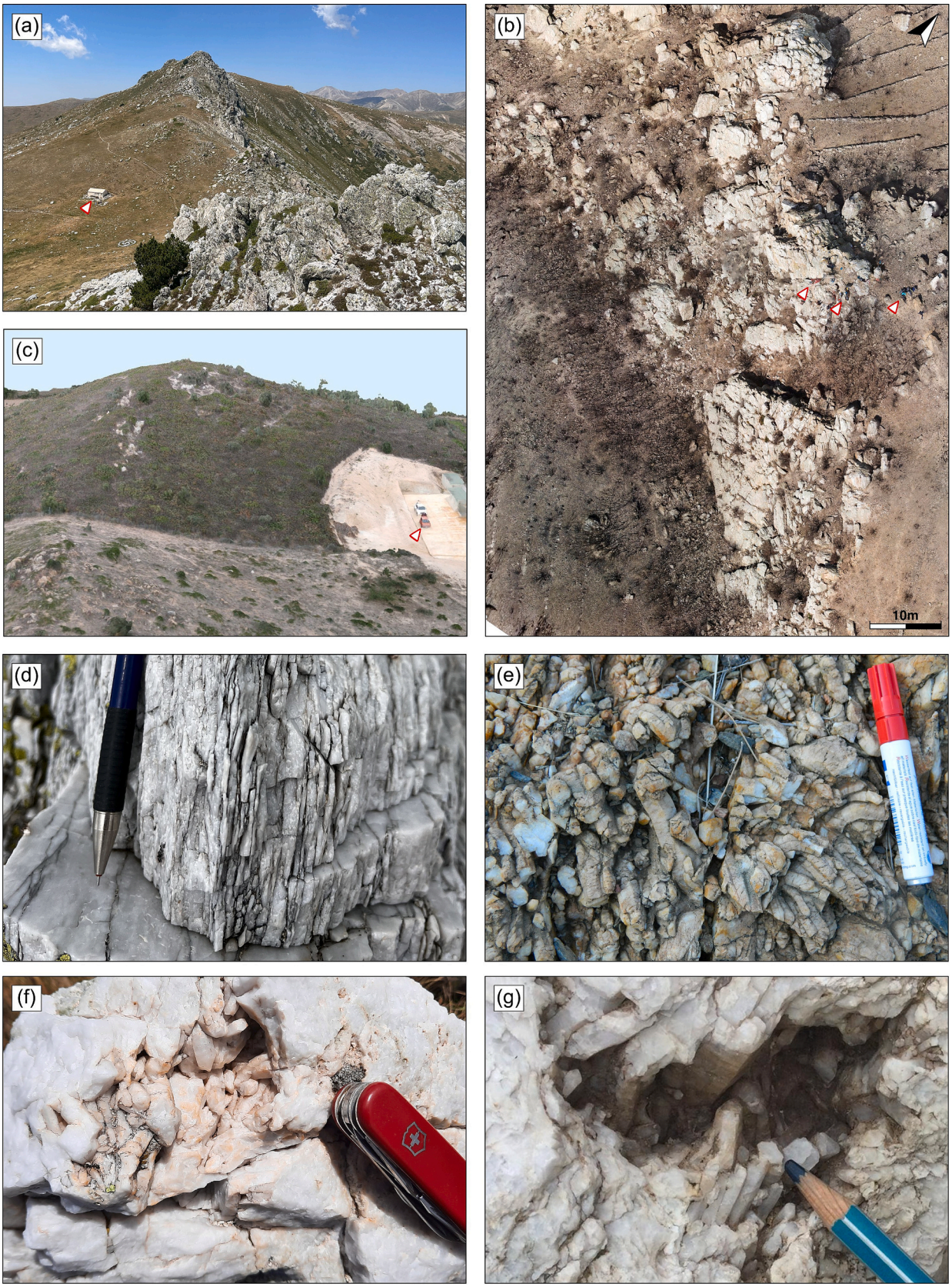

Fig. 5. Field features of the investigated giant quartz veins in the Pyrenees. (a-c) Unmanned aerial vehicle images of giant quartz vein outcrops in the Canigó (a), Cap de Creus (b), and Roc de Frausa (c) massifs; red arrows point to scale elements: a mountain shelter (a), three geologists (b), and two 4WD cars (c). (d) Detail of Type-1, deformed quartz with ENE-WSW-trending sub-vertical mylonitic bands defining a continuous foliation. (e-g) Detail of Type-2, undeformed quartz with euhedral milky to semi-transparent crystals occurring in the Cap de Creus (a), Canigó (b), and Roc de Frausa (c) massifs; note that some crystals in (e) show variable c-axis directions. (For interpretation of the references to colour in this figure legend, the reader is referred to the web version of this article.)

merged in single raster "XYZ" tiles (*MBTiles* format) using Python algorithms integrated in the QGIS software. This file format can be easily opened and interoperated (zooming in and out while preserving the desired image resolution) in many commercial and open-source GIS-based software. Furthermore, it can be uploaded to any cloud hosting service for data sharing and interactive discussion purposes. Following thin section base map creation, 1986 individual fluid inclusions were mapped as polygons and digitalized using vector based ESRI® *Shapefile* files. Topology rules were applied, when necessary, to some vector layers to detect and fix overlaps between polygons. Using the attribute table of the *Shapefiles*, a unique identification number was assigned to each polygon representing a single fluid inclusion within a categorized FIA. Information about each fluid inclusion, including their shape, phase types, phase ratios, size, FIA to which they belong, and relative timing of entrapment was recorded in a separate spreadsheet. These data were subsequently linked to the attribute table of the polygons mapped in the *Shapefile*, using the unique identification number of each inclusion. This GIS-based thin section mapping workflow provides a detailed record of petrographic observations and interpretations on fluid inclusions, allowing review of the original sample properties following destructive methods such as fluid inclusion wafer preparation, single inclusion LA-ICP-MS microanalysis, or crush-leach analysis.

Following sample mapping and fluid inclusion petrography, sample sections were cut into rectangular wafers to fit into the sample cells of the microthermometry and LA-ICP-MS systems. Heating and freezing experiments were carried out using Linkam THMSG-600 heating-freezing stages mounted on petrographic microscopes at the University of Barcelona and at RWTH Aachen University. Calibration of the stage was regularly checked using the following synthetic fluid inclusion standards: H_2O-CO_2 (CO_2 eutectic temperature: −56.6 °C), H_2O-NaCl (eutectic temperature: −21.2 °C), and H_2O (ice eutectic temperature: 0.0 °C; critical point: 374.1 °C). For determining the final ice melting temperature ($T_{m(ice)}$), final hydrohalite melting temperature ($T_{m(hh)}$), and apparent eutectic temperature (Te*), fluid inclusions were cooled down until freezing and then progressively heated up at decreasing heating rates, up to room temperature. Cyclic heating and freezing runs were required in some cases to observe the melting temperature of hydrohalite crystals. The determination of homogenization temperatures (T_h) was carried out subsequently to the Raman micro-spectroscopy and LA-ICP-MS analysis on the smallest (but measurable) inclusions of each FIA. Fluid inclusions were heated at different rates until phase homogenization. Phase transitions during freezing and heating experiments were videorecorded to ensure accuracy and increase the number of measurements during each round. The reproducibility of microthermometric experiments is estimated as 0.1 °C for $T_{m(ice)}$, $T_{m(hh)}$, and Te* measurements, and as 2 °C for T_h measurements.

Bulk fluid inclusion density and salinity of H_2O-NaCl fluid inclusions were calculated with the BULK software from the FLUIDS package (Bakker, 2003). For H_2O-NaCl-$CaCl_2$ fluid inclusions where H_2O ice was the final solid to melt, $T_{m(ice)}$ and $T_{m(hh)}$ values were used to calculate the weight fraction of NaCl relative to NaCl + $CaCl_2$ (Φ) and salinity using the equations from Naden (1996) modified by Steele-MacInnis et al. (2011). In some fluid inclusions, whose $T_{m(hh)}$ values were not measurable due to their small size, a Φ value of 0.5 was assumed as it represents the average value from those other inclusions of the FIA with a known [wt% NaCl] / [wt% NaCl + wt% $CaCl_2$] ratio. Variations of the resulting salinity as a function of the Φ value were addressed by comparing the results with neighbouring primary and pseudosecondary FIAs.

3.4. Raman micro-spectroscopy

The composition of vapor phases was evaluated in all FIAs by analysing representative fluid inclusions using Raman micro-spectroscopy (see main peaks and associated components in SM1). Between two and six Raman analyses of vapor phases for each FIA were carried out at RWTH Aachen University using a Renishaw InVia confocal Raman micro-spectrometer equipped with a Renishaw Centrus 2MYA11 detector mounted on a Leica DM2700P. Atmospheric contributions of N_2 were carefully monitored and found to be minor compared to the N_2 signals found in some of the analyzed inclusions and when comparing these to measurements of the quartz host. Calibration and laser beam accuracy was carried out daily using a silica standard. Room temperature was maintained constant at 19 °C. Spectra were collected from 100 to 4300 cm^{-1} over acquisition times of 10 s. A 488 nm edge laser at 100 % power with single accumulations was used. Acquisition setup parameters were set to extended (step scan) grating scan type, multiplicative matching, and high confocality.

3.5. LA-ICP-MS microanalysis and data reduction

The largest (i.e., > ~20 μm) fluid inclusions located at suitable depths (i.e., > ~40 μm) below the sample surface from primary and pseudosecondary FIAs were analyzed by LA-ICP-MS at RWTH Aachen University. LA-ICP-MS analyses were carried out after low-temperature microthermometry but before total homogenization temperature measurement to avoid decrepitation of fluid inclusions during heating experiments. Both inclusions previously analyzed by Raman micro-spectroscopy and those not analyzed were subsequently measured using LA-ICP-MS, showing no significant differences within individual FIAs. The analytical work was carried out using a Coherent GeolasHD 193 nm laser ablation system coupled to an Agilent 7900 quadrupole mass spectrometer with high sensitivity s-lens ion lens configuration and operated with Pt skimmer and sampler cones. No trace N_2 was added during measurements. Instrument accuracy was monitored daily by measuring the NIST SRM612 reference material as a quality control external standard against NIST SRM610, and comparing the concentrations of 36 elements across the entire mass range with those reported as reference values (Jochum et al., 2011). The instrument was tuned daily to optimize sensitivities, ensure low oxide (ThO/Th < 0.4 %) and doubly charged interference production rates (Ca^{2+}/Ca < 0.3 %) as well as stable ablation, transport, and ionization conditions (U/Th = 1.00 ± 0.02). Fluid inclusion wafers were loaded into a small volume (1 cm^3) fast-washout ablation cell based on a design from ETH Zurich that ensures high sensitivities and low detection limits. Prior to individual fluid inclusion ablation, cone-shaped holes were made at the wafer surface above the targeted inclusion by laser pre-drilling at low repetition rates (1–5 Hz) to reduce cracking and fragmentation of the quartz host and fluid inclusion leaking during the ablation. For fluid inclusion ablation, laser fluence was set at 12 J/cm^2 at a 10 Hz repetition rate. The depth-to-diameter ratio of all ablations was systematically kept below 2 to avoid depth-dependent fractionation effects (Guillong and Pettke, 2012). Accordingly, the laser beam diameter was set between 44 and 90 μm depending on the size and depth of the targeted fluid inclusion. Ablation of the host quartz and the targeted inclusion was monitored through the real-time video images of the ablation cell and the real-time (uncorrected) signals provided by the mass spectrometer for all the analyzed elements. The fluid inclusion measurements were bracketed by three analyses of two standard reference materials in order to correct for instrument drift (six standard analyses before and after every 8–12 fluid inclusion ablations). The external reference material NIST SRM610 was used for the quantification of all elements except halogens (Jochum et al., 2011). Scapolite Sca17 external standard was used for halogen quantification (Seo et al., 2011; Fusswinkel et al., 2018). Quality control tests on other halogen bearing reference materials (BB1, Kendrick, 2012) are also routinely carried out in the LA-ICP-MS laboratory. Na concentrations obtained from microthermometry were used for internal standardization.

Quantification of LA-ICP-MS results (concentrations of Li^7, B^{11}, Na^{23}, Mg^{24}, Al^{27}, Si^{29}, S^{34}, Cl^{35}, K^{39}, Ca^{44}, Ti^{47}, Mn^{55}, Fe^{57}, Cu^{63}, Zn^{66}, As^{75}, Br^{81}, Rb^{85}, Sr^{88}, Ag^{107}, Sb^{121}, I^{127}, Cs^{133}, Ba^{137}, W^{182}, Au^{197}, and Pb^{208}) was carried out using the SILLS data reduction software (Guillong et al.,

2008). This software uses the deconvolution of mineral host and fluid inclusion signals defined by the user to convert element ratios measured by LA–ICP-MS into absolute concentrations, by using the aforementioned external and internal standards. The fluid inclusion LA-ICP-MS signals were corrected for quartz host element contributions (assumed to be pure SiO_2) by bracketing each fluid inclusion signal intervals within two intervals for host correction (Fig. 6). Only fluid inclusion signals showing regular shapes, stable ablations, and synchronous elemental concentration peaks for different elements were considered (e.g., Fig. 6a-c) (e.g., Wagner et al., 2016; Fusswinkel et al., 2017; Berni et al., 2020; Tang et al., 2021). Fluid inclusion signals showing evidence for leakage (Fig. 6 d, e) or fragmentation (Fig. 6c, d, f) were not considered for element quantification (see details in Subsection 3.6). Absolute concentration values were calculated by internal standardization against salt concentrations present in the fluid phase, determined by microthermometry. Accordingly, mass balance calculations for each fluid inclusion element signal were carried out considering the FIA salinity (NaCl equivalent) and Na concentration through the common salt correction method (Allan et al., 2005). Detection limits of each analyzed element were determined using the equation from Pettke et al. (2012), yielding element concentrations at the 95 % confidence level. Charge balance calculations based on the sum of total anions and cations for each fluid inclusion element concentrations were further used after data reduction to assess the reliability of LA-ICP-MS analysis and the accuracy of fluid inclusion and background signals selection during data reduction procedures.

3.6. Data quality assessment

The microthermometric properties and elemental concentrations presented below are average values of FIAs, following the approach used during the petrographic characterization of the samples (SM1). Note that, in some cases, following this approach involves that the averaged concentrations for a given element (e.g., I for FIA IDs #3, 18, 19, 22, 30, 31, and 46) are below the averaged detection limit in the fluid inclusion dataset. For this reason, LA-ICP-MS analysis of individual fluid inclusions are also provided in the SM1. To assess the reliability of fluid inclusion data, temperatures of phase transitions obtained during microthermometry were evaluated individually and scored according to visibility conditions within the heating-freezing stage, depth, shape, and size of the inclusion, and width of the fluid inclusion boundary. During LA-ICP-MS microanalysis, scores evaluating the quality of ablations were further assigned to each analysis based on qualitative observations made in real-time video images of the ablation cell and signals provided by the mass spectrometer.

The reliability of LA-ICP-MS analyses was further evaluated during the data reduction process (Fig. 6) (Pettke, 2008; Fusswinkel et al., 2017). Ablations were considered successful when the ablation of the host mineral before and after the inclusion provided relatively stable and steady signals (Fig. 6a-c, g). Signals related to fluid inclusion leakage (i.e., fracture formation at the bottom of the ablation pit and non-instantaneous release of the inclusion content; Fig. 6e, f) or fragmentation (i.e., uncontrolled opening of the inclusion cavity and explosive fluid release; Fig. 6d, f) were not considered for elemental quantification, since both may produce a biased sampling of inclusion contents in the mass spectrometer. Analysis of individual fluid inclusions with inconsistent element/Na ratios when compared to values from other inclusions within the same FIA were also assumed as resulting from leakage or fragmentation processes, or non-representative sampling upon inclusion breach (Heinrich et al., 2003), and thus not considered. Charge balance calculations between cations and anions after element quantification with the mass balance approach (Allan et al., 2005) were also used to corroborate charge neutrality of the LA-ICP-MS results. Sometimes, two or more fluid inclusion signals were obtained during a single ablation (Fig. 6d, e, g, h). For these cases, before considering all signals during data reduction in the SILLS software, the ablated area was examined in the GIS-based thin section maps to determine if all the fluid inclusion signals obtained during the ablation belong to the same FIA (Fig. 6d, e) or not (Fig. 6h). The occurrence of several of the aforementioned signal types within a single ablation sometimes made the data reduction process a demanding task in terms of spike elimination and fluid inclusion and host quartz signal selection (Fig. 6d, e). Iodine signal during fluid inclusion ablation was sometimes absent or very weak (Fig. 6e), whilst in other cases was clearly above the background signal (Fig. 6g). The resulting dataset (see SM1) includes petrographic descriptions, averaged microthermometry results, Raman peaks of 50 FIAs, and the reliable elemental compositions obtained from LA-ICP-MS microanalysis of 36 primary and pseudosecondary FIAs. Scores assigned during either microthermometry or LA-ICP-MS microanalysis were subsequently used to evaluate outliers.

4. Results

4.1. Fluid inclusions systematics

In the three studied massifs (Figs. 1–4), fluid inclusions have been identified in the Type-1 deformed quartz and in the Type-2 euhedral quartz crystals that are present in cavities. GIS-based fluid inclusion petrography coupled with EBSD analyses reveal that those inclusions present in theType-1 deformed quartz (Fig. 5d) are mostly affected by post-entrapment modification such as leaking and partial to complete decrepitation (Fig. 7a) (e.g., Bodnar, 2003). This is further confirmed by inconsistent, highly variable phase proportions within the same FIAs. Quartz deformation in the Type-1 samples mainly occurred by dislocation creep (subgrain rotation regime) and, accordingly, stretching may be envisaged as the dominant mechanism of fluid inclusion post-entrapment modification (Fig. 7a) (e.g., Vityk et al., 2000). Additionally, diffusion creep microstructures, such as those resulting from pressure-solution of quartz grains and cataclastic grain-size reduction bands, are present in the Type-1 quartz and are associated with fluid inclusions modification. These processes have been observed in all measurable inclusions within the Type-1 quartz, independently of their size (Fig. 7a). Therefore, petrography, microthermometry, and LA-ICP-MS analyses have been focused on the FIAs present in the undeformed Type-2 host quartz (Figs. 5e-g, 7b). This quartz assemblage shows significantly less intra-granular crystal-plastic deformation and, therefore, more reliable FIAs (see EBSD maps of Grain Reference Orientation Deviation (GROD) angles, where areas with high intracrystalline deformation appear in red-yellow colours; Fig. 7).

FIAs identified within the cover- and basement-hosted Type-2 euhedral quartz show relatively similar petrographic features in the three study areas (Figs. 1–4, 8). The host quartz is always milky to semi-transparent and shows growth bands defined by primary fluid inclusions (Fig. 8). Quartz crystals cut normal to the c-axis direction show inclusions often clustering in the core and outer growth bands (Fig. 8a). Between the core and the outer growth bands, only pseudosecondary fluid inclusion trails are present (Fig. 8a). Most inclusions are liquid-rich and aligned in parallel to sub-parallel growth bands (Fig. 8b-g), sometimes associated with the position of particular growth faces (Fig. 8g). In sections cut parallel to the c-axis direction, primary fluid inclusions in a particular growth face are always arranged following the same direction, which can be semi-parallel (Fig. 8b) or at high angle (Fig. 8d, f) to pseudosecondary trails formed by smaller inclusions. These pseudosecondary FIAs do not cut across all growth bands of the crystal and are always truncated by alignments of primary inclusions at the growth zone boundaries (Fig. 8b, d, f). Sometimes, fluid inclusions within growth bands show growth spurs with flat bases and tapering tips, narrowing towards the direction of crystal growth, or they are elongated along the direction of crystal growth (Fig. 8f). Secondary fluid inclusions are found in linear arrays that cut across all growth zones of a crystal, following intragranular, or more often transgranular healed fractures (Fig. 8e). In most cases, the angle between the directions of primary and

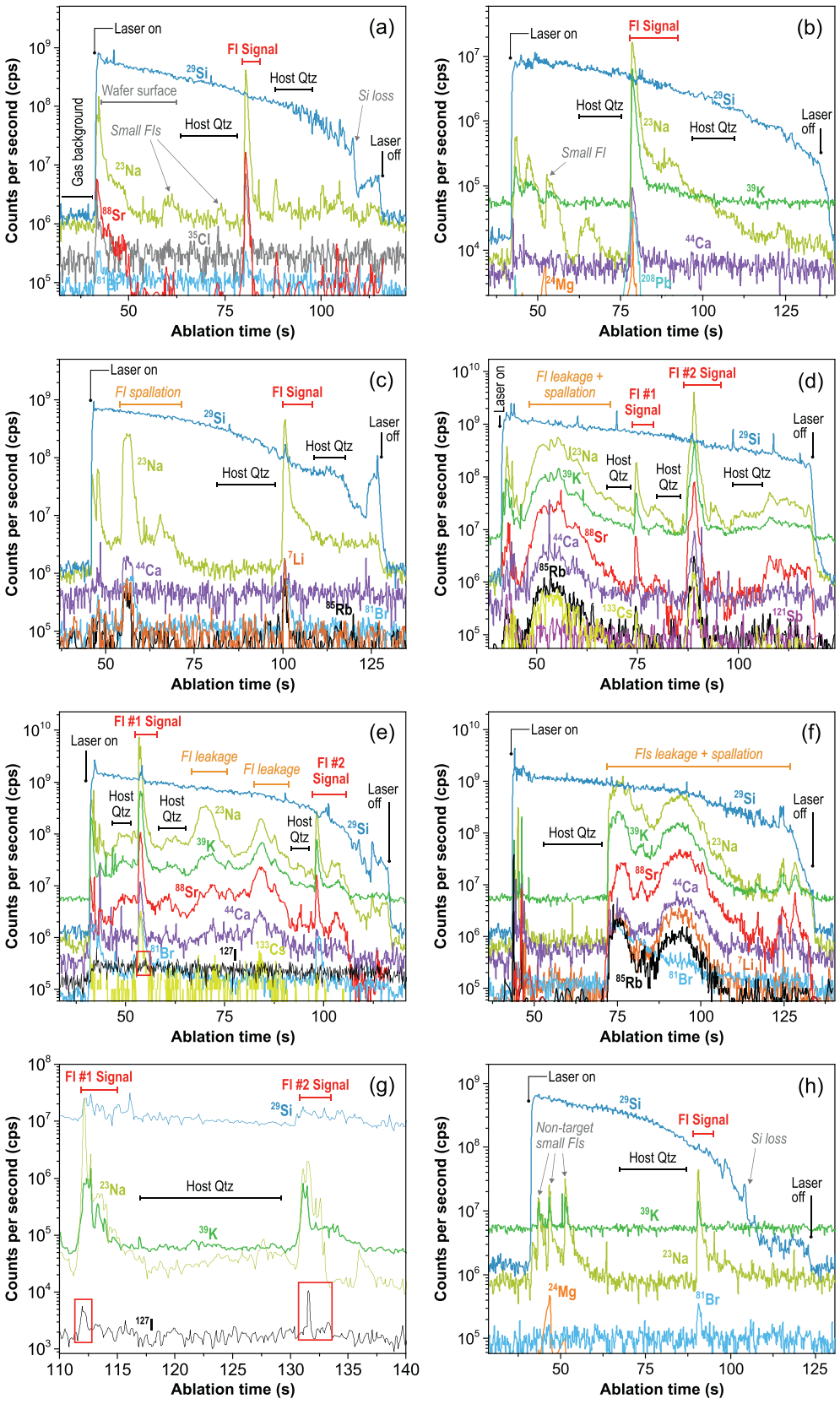

(caption on next page)

Fig. 6. Selected examples of time-resolved fluid inclusion LA-ICP-MS signals. Annotations correspond to gas background, laser on/off, and time windows for host rock correction and fluid inclusion quantification used during data reduction. (a, b) Successful ablations of large (> 30 μm) fluid inclusions at ca. 80 s; host rock signals are relatively stable; individual element signals are synchronous with the Na peak used for internal standardization; small fluid inclusions located above the target were hit by the laser providing low-quality signals. (c, d) A first unstable bell-shaped signal with spiky patterns reflects fragmentation and leakage processes in near-surface fluid inclusions hit at the very beginning of the ablation; later on, during the ablation, host signals become stable; the target inclusion is hit at ca. 100 s in (c); two reliable signals from the same FIA are obtained in (d). (e) Successful ablation with a high-intensity signal at the beginning of the ablation (ca. 53 s), subsequently followed by two bell-shaped spiky signals related to the leaking of small fluid inclusions; a second reliable signal is obtained just before the end of the ablation; the red box indicates the (weak) Iodine signal obtained from this inclusion. (f) Unsuccessful ablation due to crack formation that produced leakage and fragmentation, giving rise to a stepwise release of the inclusion content with unstable long-lasting signals. (g) Zoom into the 110–140 s time interval of a successful ablation of two fluid inclusions; Iodine (red boxes) yield a significant signal above background for both signals. (h) Low-intensity but well-defined signals of small (> 30 μm) fluid inclusions hit at the very beginning of the ablation; according to GIS-based fluid inclusion petrography, these inclusions do not belong to the target FIA and were thus not considered; subsequently, the target inclusion is hit at ca. 90 s providing a reliable signal. For clarity purposes, only selected elements are shown in all panels. (For interpretation of the references to colour in this figure legend, the reader is referred to the web version of this article.)

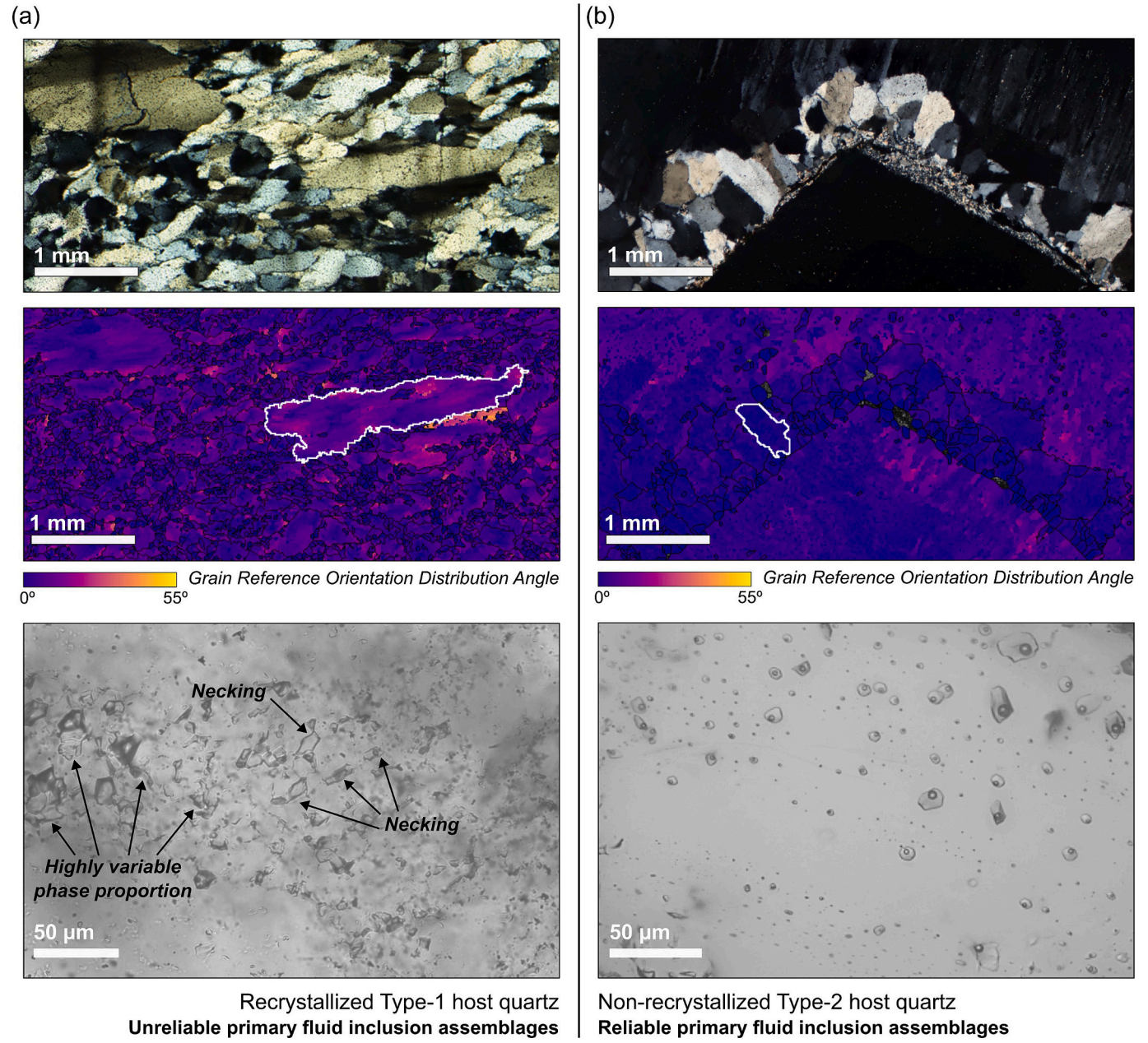

Fig. 7. Comparative qualitative evaluation of fluid inclusion reliability depending on the type of host quartz where they occur. (a) Type-1 host quartz has experienced significant ductile deformation and shows evidence of dynamic recrystallization through subgrain rotation in the crossed-polars microphotograph (top); Grain Reference Orientation Distribution (GROD) maps, obtained through Electron Backscatter Diffraction, reveal areas with significant intracrystalline deformation (high angles, reddish-yellowish colours) respect to the average angle of each grain (middle); Fluid inclusions in these areas show reequilibration evidence and, accordingly, are interpreted as unreliable for any fluid inclusion study (bottom). (b) Type-2 host quartz shows euhedral crystals without significant deformation evidence under crossed-polars (top); GROD maps reveal very low intracrystalline deformation (low angles, blueish colours) throughout the investigated area (centre); Fluid inclusions in this scenario (bottom) show regular shapes, consistent phase proportions without evidence of reequilibration, being thus considered as reliable for further investigations.

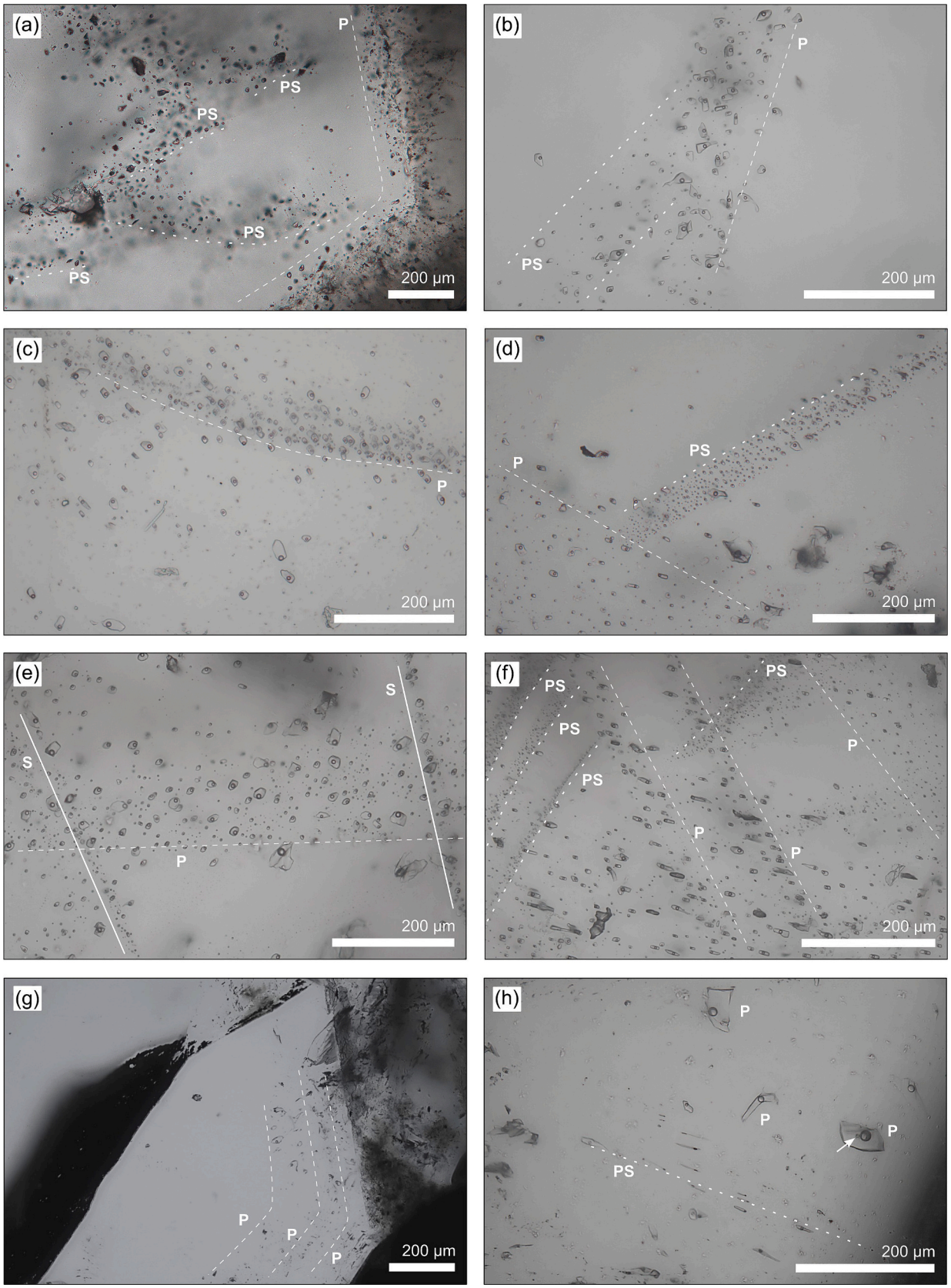

Fig. 8. Representative focus-stacked microphotographs of Primary (P), Pseudo-secondary (PS) and Secondary (S) aqueous two-phase fluid inclusion assemblages within the investigated samples (plane-polarized light). (a-d) Crystal growth bands show alignments of primary fluid inclusions that often represent the end areas of pseudosecondary fluid inclusion trails. (e) Intra-granular and trans-granular secondary fluid inclusion trails cut across all growth zones of the crystal. (f) Primary fluid inclusions are often elongated following the crystal growth direction. (g, h) Largest (ca. 60–100 µm) primary fluid inclusions often occur in specific crystal growth faces; white arrow indicates a trapped solid phase within a large inclusion.

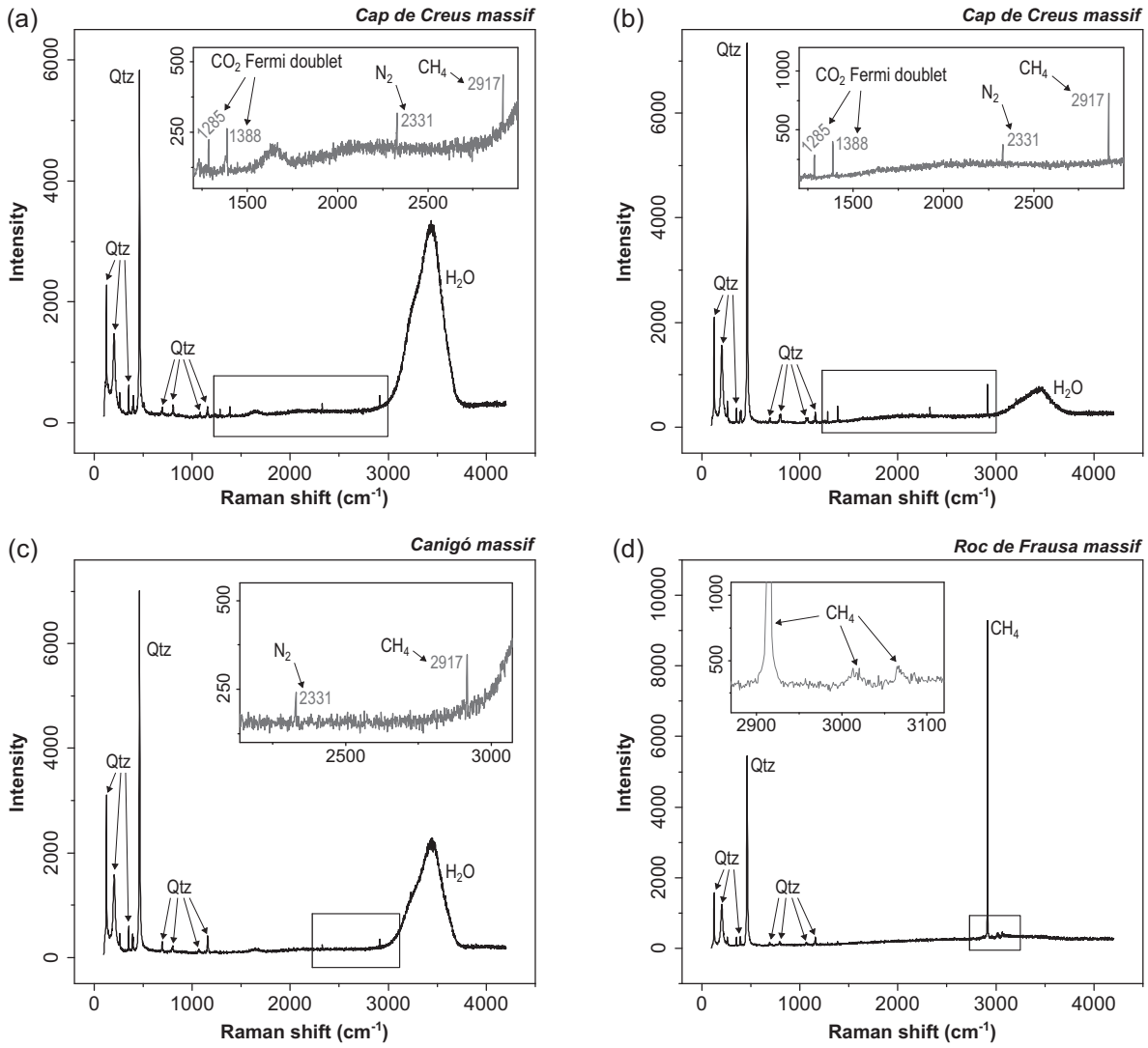

Fig. 9. Representative Raman micro-spectroscopy signals of the vapor phases in fluid inclusions from the Cap de Creus (a, b), Canigó (c), and Roc de Frausa massifs. Minor amounts of N_2, CO_2, and CH_4 gaseous phases are obtained for the H_2O-dominated fluid inclusions within the basement-hosted Type-2 quartz (a-c). CH_4 is the main gaseous phase in fluid inclusions within the cover-hosted Type-2 quartz (d).

secondary FIAs is high (> 40°) and, therefore, the origin and relative timing relationships of both are clearly distinguishable by petrography. Rarely, crystals show an apparently random three-dimensional arrangement of fluid inclusions when examined along the z direction and, therefore, the relative timing relationships of fluid inclusions cannot be determined.

Fluid inclusion sizes are variable within each FIA (e.g., Fig. 8e). The largest inclusions (e.g., Fig. 8g, h) located at suitable depths below the sample surface were pre-selected during petrographic descriptions to be employed for freezing experiments and LA-ICP-MS microanalysis. All FIAs in the three study areas (Figs. 1–4) are composed of two-phase LV-type aqueous fluid inclusions with regular shapes. Most of them have sizes of 20–45 μm and a vapor phase proportion of ca. 10 vol% (L10V) at room temperature (Fig. 8). The phase proportions are always consistent within the same FIA (e.g., Fig. 8e, h). Rarely, trapped solid phases are present within some of the largest inclusions (Fig. 8h).

4.2. Fluid inclusions microthermometry and Raman micro-spectroscopy

Raman micro-spectroscopy and heating-freezing experiments were carried out respectively in 138 and 909 representative primary and pseudosecondary fluid inclusions (Figs. 9, 10). Despite being petrographically similar, FIAs representing basement- and cover-hosted fluids within the Type-2 quartz show significant variations in their fluid systems, composition of vapor phases, and salinities, which are described below.

In the basement-hosted Type-2 quartz from the Cap de Creus (FIA IDs #1–33; SM1) and Canigó (FIA IDs #40–50; SM1) massifs (Figs. 2, 3), all FIAs are formed by a liquid phase dominated by H_2O-NaCl-$CaCl_2$ fluids. This is indicated by the occurrence of the first visible liquid phase (apparent eutectic temperature, Te*) between −40 and −36 °C. Raman micro-spectroscopy measurements reveal that vapor phases of basement-hosted inclusions are mostly formed by H_2O(g) (Fig. 9a-c) and, sometimes, minor proportions (with weaker Raman shift intensities) of CO_2(g) (Fermi doublet peaks at 1285 and 1388 cm^{-1}; Fig. 9a, b), CH_4(g) (peak at 2917 cm^{-1}; Fig. 9a-c), and N_2(g) (peak at 2331 cm^{-1}; Fig. 9a, b). During heating of frozen inclusions, ice is the most common phase observable. Hydrohalite crystals were sometimes indistinguishable upon initial observation, but exhibited noticeable enlargement following temperature cycling. Hydrohalite was always the first phase to melt during heating, yielding $T_{m(hh)}$ between −28 and −24 °C. Ice was the last phase to melt and yield $T_{m(ice)}$ between −19 and −11 °C in samples from the Cap de Creus massif (Fig. 10a). Significantly higher $T_{m(ice)}$ values, between −13 and −7 °C, were obtained from samples of the Canigó massif (Fig. 10b).

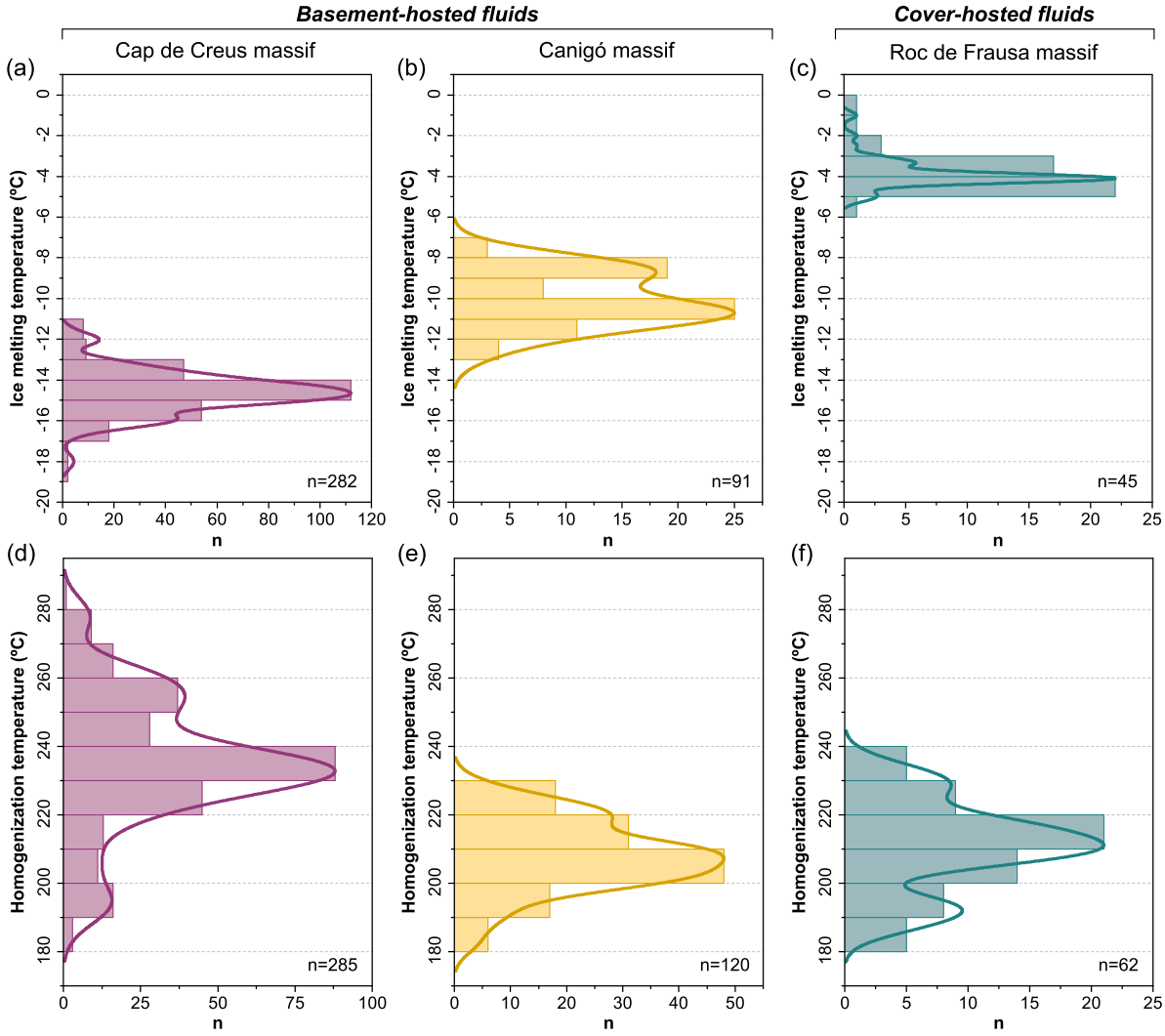

Fig. 10. Histograms and Kernel Distribution Estimates of (a-c) Ice Melting Temperatures ($T_{m(ice)}$) and (d-f) Homogenization Temperatures (T_h) of two-phase aqueous fluid inclusions within the basement- (Cap de Creus and Canigó massifs) and cover-hosted (Roc de Frausa massif) Type-2 quartz. Individual FIA averages and their corresponding 1σ standard deviations are provided the Supplementary Material 1.

These phase transition temperatures correspond to salinities from 15.7 to 19.1 wt% $NaCl_{eqv}$ for the Cap de Creus massif and from 12.7 to 15.6 wt% $NaCl_{eqv}$ for the Canigó massif (Fig. 11). Fluid inclusions from the Cap de Creus massif homogenize into the liquid phase (LV → L) at temperatures of 180–280 °C (Fig. 10d). Homogenization temperatures (LV → L) in samples from the Canigó massif are within those values obtained for the Cap de Creus massif, but significantly clustered in a narrower interval between 180 and 230 °C (Fig. 10e).

Fluid inclusions in the cover-hosted Type-2 quartz from the Roc de Frausa massif (FIA IDs #34–39) (Fig. 4) are liquid-vapor inclusions dominated by H_2O-NaCl liquid, as indicated by Te* values from −20 to −12 °C. The vapor phase contains dominantly CH_4(g) (Raman peaks at 2917, 3020, and 3066 cm^{-1}) (Fig. 9d). Since CH_4 was only found within the gas phase and no clathrates occurred during freezing experiments, the density of the carbonic phase was assumed to be negligible and thus ignored for salinity calculations. Ice was the only phase observable during the heating of frozen inclusions and yield $T_{m(ice)}$ values from −1 to −5.9 °C with a maximum in the frequency distribution around −5 to −3 °C (Fig. 10c). The measured phase transition temperatures correspond to salinity values from 4.8 to 7.2 wt% $NaCl_{eqv}$ (Fig. 11). Cover-hosted fluid inclusions also homogenize into the liquid phase (LV → L) at temperatures ranging from 180 to 240 °C with a maximum in the frequency distribution at ca. 210 °C (Fig. 10f).

In all cases, measured FIAs from each study area define symmetric or partially skewed unimodal distributions of T_h and $T_{m(ice)}$ when considered altogether (Fig. 10). Moreover, all analyzed fluid inclusions within a given FIA show consistent values whose variation is $< \pm 11$ °C for the T_h values and $< \pm 1.5$ °C for either $T_{m(ice)}$ and $T_{m(hh)}$ values. FIA averages and 1σ standard deviations of microthermometric data are provided in the SM1. A graphical summary with more than 200 photomicrographs at different stages of the freezing rounds for each studied FIA is provided in the SM2.

4.3. LA-ICP-MS fluid inclusion microanalysis

The reconstructed fluid compositions after microthermometry, Raman spectroscopy, and LA-ICP-MS fluid inclusion microanalysis are summarized in Table 1. Average elemental concentrations of the investigated FIAs are provided in Figs. 12 and 13 and in the SM1. Most FIAs have consistent average concentrations of all analyzed elements, as indicated by small 1σ standard deviations. Exceptions are only shown for Fe, Cu, S, and I concentration averages of a few (< 5) basement-hosted FIAs (Figs. 12, 13). When comparing different FIAs from the same study area, element concentrations show values within the standard deviation or one order of magnitude. Although the entire dataset is very consistent, few outlying data are present. For example,

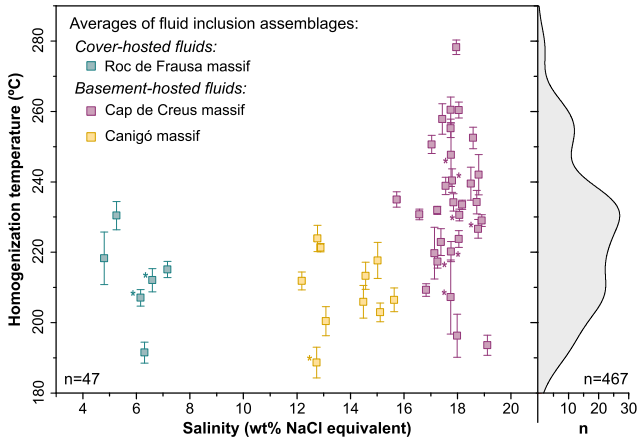

Fig. 11. Homogenization Temperatures (T_h) vs. Salinity plot of primary and pseudosecondary fluid inclusion assemblages (FIAs) from the basement- (Cap de Creus and Canigó massifs) and cover-hosted (Roc de Frausa massif) Type-2 quartz. Data points are FIA averages representing between 8 and 15 measurements of individual fluid inclusions. The standard deviation of the salinity for each FIA is smaller than the symbol size. Individual FIA averages and their corresponding 1σ standard deviations are provided the Supplementary Material 1. A Kernel Distribution Estimate for the T_h average values is included for clarity in the right-side of the diagram. Data points labelled with '*' represent FIAs that yielded unreliable LA-ICP-MS signals and were not considered for elemental concentration quantification (see data quality constraints in Section 3.6).

concentrations of Al, Ag, Ti, and Mg of the FIA ID#26 are much higher than those of other FIAs of the same sample (Fig. 13). Furthermore, FIA ID#28 has lower Cu values (Fig. 12) and FIA ID#45 higher Li concentrations (Fig. 13). All these outlying data met the data quality criteria defined in Subsection 3.6 and were thus considered. These variations are therefore assumed to represent true variations of the fluid trace metal concentrations depending on the relative timing of entrapment of FIAs.

Systematic variations in the average elemental concentrations of FIAs can be identified when comparing the different study areas (Cap de Creus, Canigó, and Roc de Frausa; Fig. 1) and their orogenic setting (basement and cover rocks; Figs. 2–4). Major elements showing highest concentrations ($> 10^4$ μg/g) in the three areas are Cl, Ca, Na, K, and S. Sometimes, Ca contents inferred from microthermometry are slightly higher (and Na/Ca ratios are thus lower) when compared with those derived from LA-ICP-MS data (see SM1). This discrepancy may stem from uncertainties in determining phase transitions during microthermometry (e.g., hydrohalite melting temperatures). It could also be related to the presence of additional cations (e.g., K as revealed by FIA concentrations), since the experimental data on freezing point depression in multisolute systems is only available for binary (e.g., H_2O-NaCl) or ternary (e.g., H_2O-NaCl-KCl, H_2O-NaCl-$CaCl_2$) systems. Overall, we base our interpretations on the more robust LA-ICP-MS results for discussing below the fluid evolution.

Basement-hosted fluids show systematically higher concentrations of K, Ca, Cl, Cs, Sr, and Br, whereas cover-hosted fluids are characterized by an enrichment in B, Cu, Sb, Li, Pb, Zn, Ti, Ba, Mg, Rb, and I (Table 1). By contrast, the average concentrations of Au, W, Fe, Mn, and S do not show systematic enrichment/depletion patterns as a function of the structural setting. Within the basement-hosted fluids, concentration variations depending on the study area are also present. Fluids from the Canigó massif generally show higher Al, Mg, W, and Cu concentrations and are vaguely depleted in Sr, Cs, and K, when compared with Cap de Creus massif fluids (Figs. 12, 13).

Many transition metals, as well as alkali and alkaline earth metals, form strong chloride complexes in aqueous solution. Therefore, Cl-normalized element mass ratio bivariate plots (Figs. 14, 15a-c) are best suited to remove the effects of chlorinity, allowing the evaluation of the relationship between metal concentrations (e.g., Yardley, 2005). Element mass ratio diagrams as a function of FIA salinity (Fig. 14) show that the low-salinity cover-hosted fluids are systematically enriched in highly and moderately fluid-compatible base metals such as Fe (Fig. 14a), Cu (Fig. 14b), Pb and Zn (Fig. 14c), as well as in Mg (Fig. 14d), when compared to basement-hosted fluids. This enrichment is up to one order of magnitude for the Cu/Cl (Fig. 14b) and Pb/Cl + Zn/Cl (Fig. 14c) mass ratios but is significantly lower for Fe/Cl (Fig. 14a) and Mg/Cl (Fig. 14d). By contrast, cover-hosted fluids are depleted with respect to basement-hosted fluids in some alkali and alkaline earth metals such as Sr (Fig. 14e), Cs (Fig. 12), and K (Fig. 12), as well as in Br (Fig. 14f). Both basement- and cover-hosted fluids show significant variations in their mass ratios even when comparing samples within the same study area. Variations in Cu/Cl and Mg/Cl for the Cap de Creus are, for example, in the range of two orders of magnitude. Cover- and basement-hosted fluids fall in a rather narrow range in Fig. 14d, e, indicating essentially constant mass ratios of Mg/Cl for the cover-hosted and of Sr/Cl for the basement-hosted fluids.

The Rb/Cl vs. Li/Cl diagram (Fig. 15a) shows that basement-hosted fluids form a uniform cluster and thus have constant alkaline metal concentrations, which are significantly lower than those in the cover-hosted fluids that show also a wider variability. No systematic differences in ore metal concentrations have been identified for cover- and basement-hosted fluids. This can be clearly seen by the wide distribution of data points (spanning two to three orders of magnitude) in the Sb/Cl vs. W/Cl (Fig. 15b) and Au/Cl vs. Ag/Cl (Fig. 15c) diagrams. However, with some exceptions, the cover-hosted fluids appear to have higher Sb, W, Au, and Ag contents (Fig. 15b, c). Substantial amounts of B have also been analyzed in samples from the three studied sectors, with the cover-hosted fluids showing the highest concentrations (Fig. 15d), and will be discussed below.

Table 1
Summary of the reconstructed fluid compositions from the three investigated areas. Major and relevant trace elements indicated are those representing the main fluid composition and thus used for discussion on fluid evolution. Other trace elements disregarded do not show noteworthy systematic variations as a function of the structural setting; see Figs. 12 and 13 for complete concentration summaries and Supplementary Material 1 for raw data.

Orogenic Setting (Area)	Salinity (wt% eq. NaCl)	T_h (°C)	Gas phase components	Major elements	Relevant trace elements	I/Cl (molar)	Br/Cl (molar)	Br/I (molar)
Basement (C. de Creus)	16–20	190–260	H_2O(g)	Na, Ca, K (Mg, Fe)	Cs, Sr, Br	1.10E-05 - 3.14E-04	2.89E-03 - 1.11E-02	2.48E+01–4.98E+02
Basement (Canigó)	12–16	190–220	H_2O(g)			1.91E-05 - 4.28E-04	4.50E-03 - 8.79E-03	1.41E+01–2.73E+02
Cover (R. de Frausa)	4–7	180–240	H_2O(g), [CH_4(g)]	Na (Ca, K, Mg, Fe)	Cu, Sb, Pb, Zn, Ti, Rb, B, Ba, Rb, Li, I	1.07E-04 - 4.28E-04	1.84E-03 - 3.69E-03	7.76E+00–1.73E+01

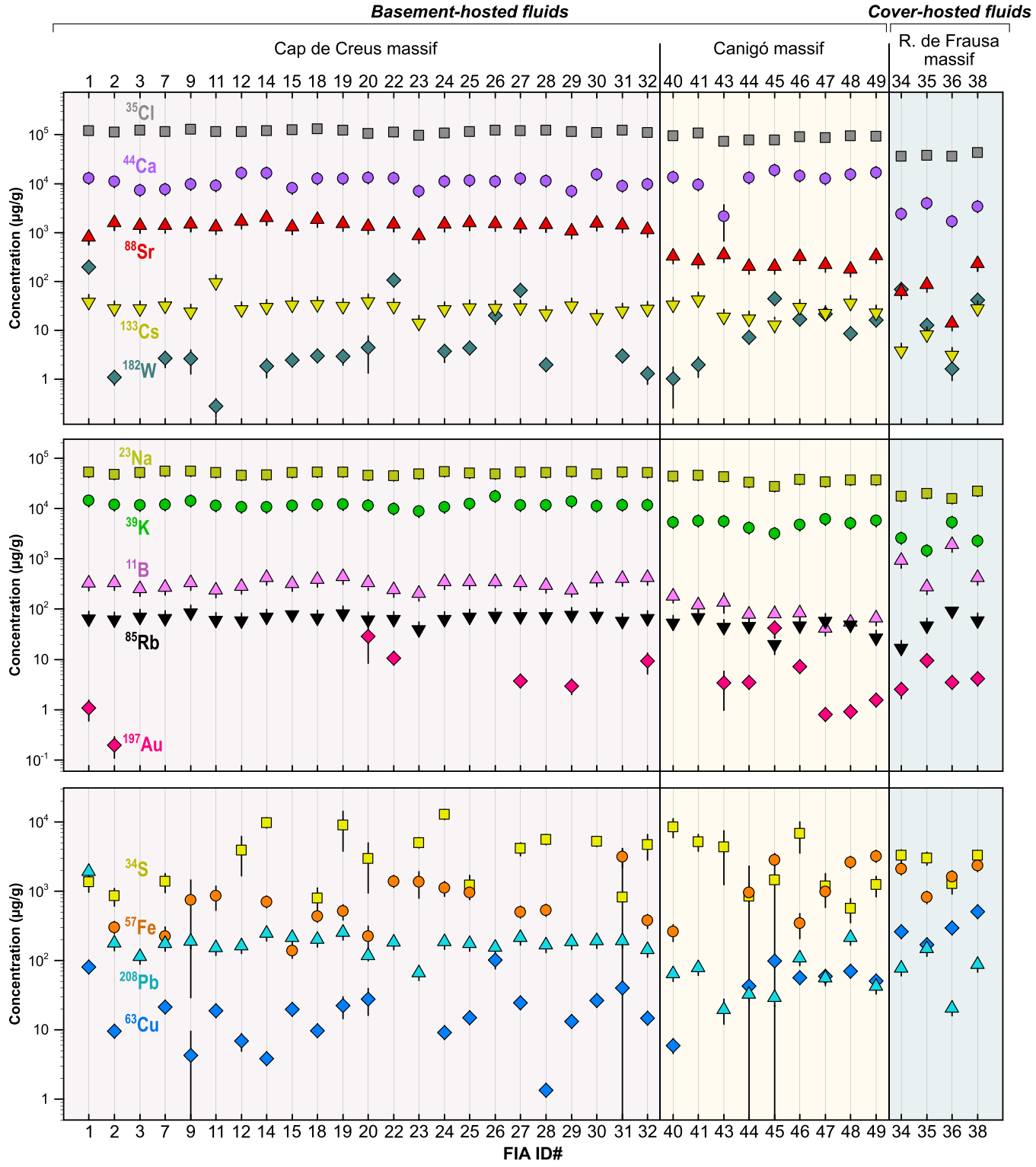

Fig. 12. Summary of the elemental concentrations of Cl, Ca, Sr, Cs, W, Na, K, B, Rb, Au, S, Fe, Pb, and Cu obtained through LA-ICP-MS microanalysis of individual fluid inclusions from the basement- (Cap de Creus and Canigó massifs) and cover-hosted (Roc de Frausa massif) Type-2 quartz. Data points are fluid inclusion assemblage (FIA) averages representing between 2 and 20 analysis of individual fluid inclusions. The final number of measurements has depended on sample and FIA characteristics, ablation conditions, and LA-ICP-MS data reduction constraints (see text for explanation). Individual FIA averages and their corresponding 1σ standard deviations are provided the Supplementary Material 1.

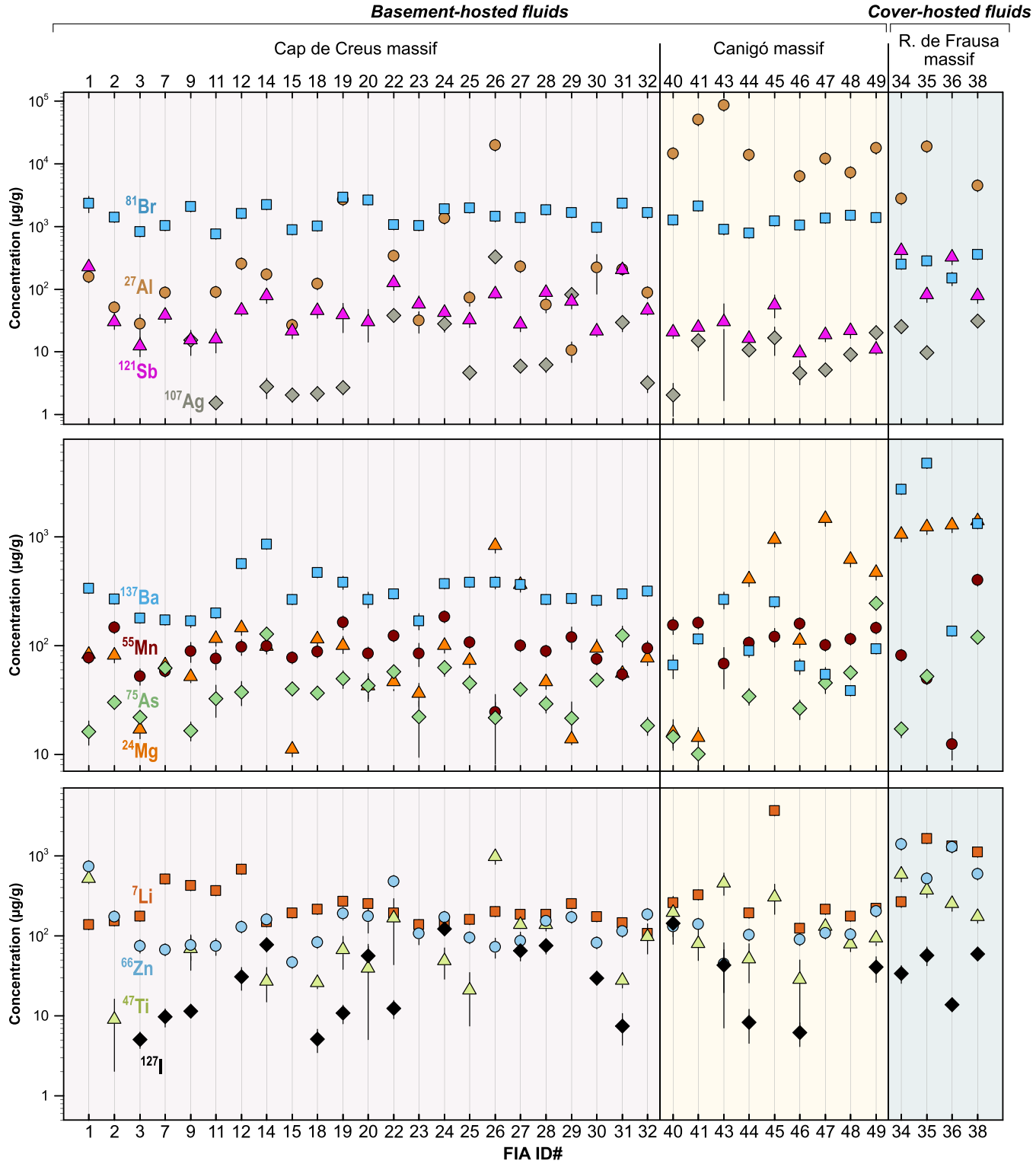

Fig. 13. Summary of the elemental concentrations of Br, Al, Sb, Ag, Ba, Mn, As, Mg, Li, Zn, Ti, and I obtained through LA-ICP-MS microanalysis of individual fluid inclusions from the basement- (Cap de Creus and Canigó massifs) and cover-hosted (Roc de Frausa massif) Type-2 quartz. Data points are fluid inclusion assemblage (FIA) averages representing between 2 and 20 analysis of individual fluid inclusions. The final number of measurements has depended on sample and FIA characteristics, ablation conditions, and LA-ICP-MS data reduction constraints (see text for explanation). Individual FIA averages and their corresponding 1σ standard deviations are provided the Supplementary Material 1.

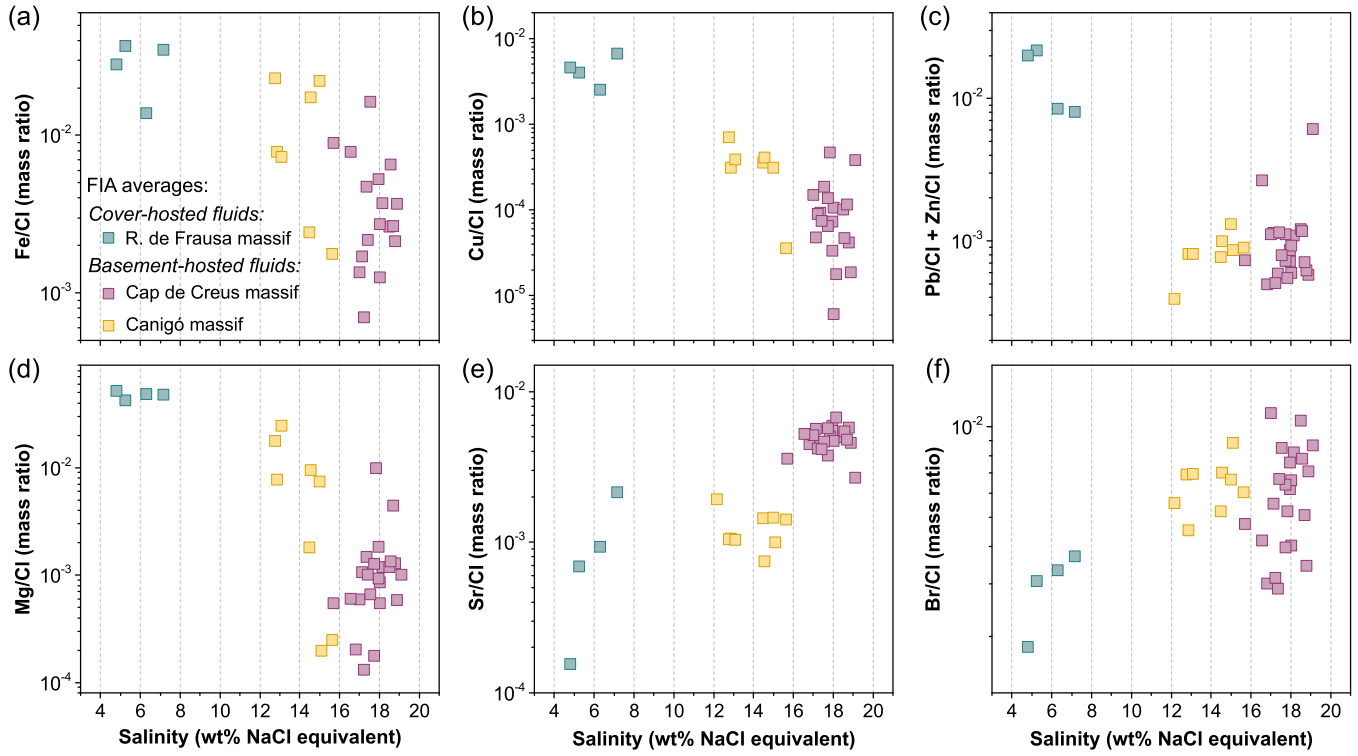

Fig. 14. Representative variation diagrams of Cl-normalised fluid inclusion assemblage (FIA) average element concentrations (in mass ratio), as function of FIA salinity: (a) Fe/Cl, (b) Cu/Cl, (c) Pb/Cl + Zn/Cl, (d) Mg/Cl, (e) Sr/Cl, and (f) Br/Cl. Individual FIA averages of elemental concentrations and their corresponding 1σ standard deviations are provided Figs. 12 and 13 and in the Supplementary Material 1.

5. Discussion

5.1. Triple-halogen data: usefulness and significance

Halogen fractionation in natural systems is limited to specific processes such as evaporation (passively increasing the Bromine and, to a lesser extent, the Iodine content in the residual fluid), evaporite dissolution (selectively increasing the Chlorine content), and organic matter interaction (where the organic matter loses Bromine and Iodine to the fluid) (Richard et al., 2014; Wilkinson, 2014; Kendrick, 2018; Pirajno, 2018). Conversely, fluid-rock interaction does not generally alter Cl, Br, and I concentrations and their ratios. Exceptions have been only reported during fluid-rock interaction in meta-gabbros (Kendrick et al., 2005) or eclogite-facies metamorphism of granulites (Svensen et al., 1999), following preferential incorporation of Cl into amphibole under low water-rock ratios. These rocks are, however, absent in the three investigated areas. Therefore, triple-halogen (Cl, Br, and I) concentrations can be considered as excellent fluid provenance tracers (Ridley and Diamond, 2000; Fu et al., 2012; Kendrick, 2018; Pirajno, 2018). Past studies of halogen compositions of different fluid types have mostly been based on bulk sample methods such as combined noble gas and halogen analyses, crush-leach ion chromatography or solution ICP-MS (e.g., Kendrick and Burnard, 2013). Since these bulk sample methods do not permit a petrographic control of the analyzed FIAs, they may result in averaged compositions skewed towards the fluid inclusion types containing high concentrations of any given element. By contrast, LA-ICP-MS fluid inclusion microanalysis provides full petrographic control of the sampled fluids, making it possible to resolve compositionally distinct fluid characteristics on the sample scale (e.g. Wagner et al., 2016), and can also be used for quantification of halogen concentrations for Cl, Br, and I (Fusswinkel et al., 2018).

The dataset reported in this paper, obtained for both basement- and cover-hosted fluids in a well-studied area, shows that halogen signatures of fluids that formed Pyrenean GQVs vary significantly within an apparently homogeneous environment (Fig. 16). The most significant halogen concentration variations are found in the I/Cl ratios of the basement-hosted fluids at Cap de Creus and Canigó massifs (Fig. 16a). Their halogen data is consistent with residual basinal brines originating from seawater and having undergone some degree of evaporation and subsequent organic matter interaction (Kendrick et al., 2005; Scharrer et al., 2023). A key data observation is the variation in Br/I ratios (diagonal lines in Fig. 16) within Cap de Creus and Canigó massifs FIAs along a compositional trend. The observed variation is well outside the range of analytical uncertainty and we interpret it as being consistent with mixing between two fluid endmembers, one of which underwent a higher degree of organic matter interaction prior to mixing and quartz vein formation. FIAs with IDs #22 and 24 (Fig. 16; SM1), which belong to the same sample but show substantially different Br/I ratios, are good indicators of this possibility. The trajectory of the data array and the increase in the Br/Cl ratio relative to seawater indicates that both fluids would have originally been residual evaporite fluids after a moderate degree of evaporation, and that they may thus share a common source. It is well established that basinal brines readily infiltrate deep into basement lithologies. Fluid signatures within the basement can then become compositionally stratified as overlying sedimentary environments change over time and lead to infiltration of various basinal fluid types (Bons and Gomez-Rivas, 2013, 2020; Bons et al., 2014; Fusswinkel et al., 2014; Scharrer et al., 2021). Seismic events causing fault activation and fluid flow can then lead to tapping of these compositionally distinct fluids in mixing zones within the basement, without invoking hydrologically impossible scenarios such as simultaneous upwards and downwards flow (see Bons et al., 2014). The halogen compositional trend observed in Cap de Creus and Canigó fluids could thus be interpreted as mixing of compositionally distinct fluid endmembers tapped from different sources within the basement, agreeing with the relatively large variation of fluid inclusion homogenization temperatures,

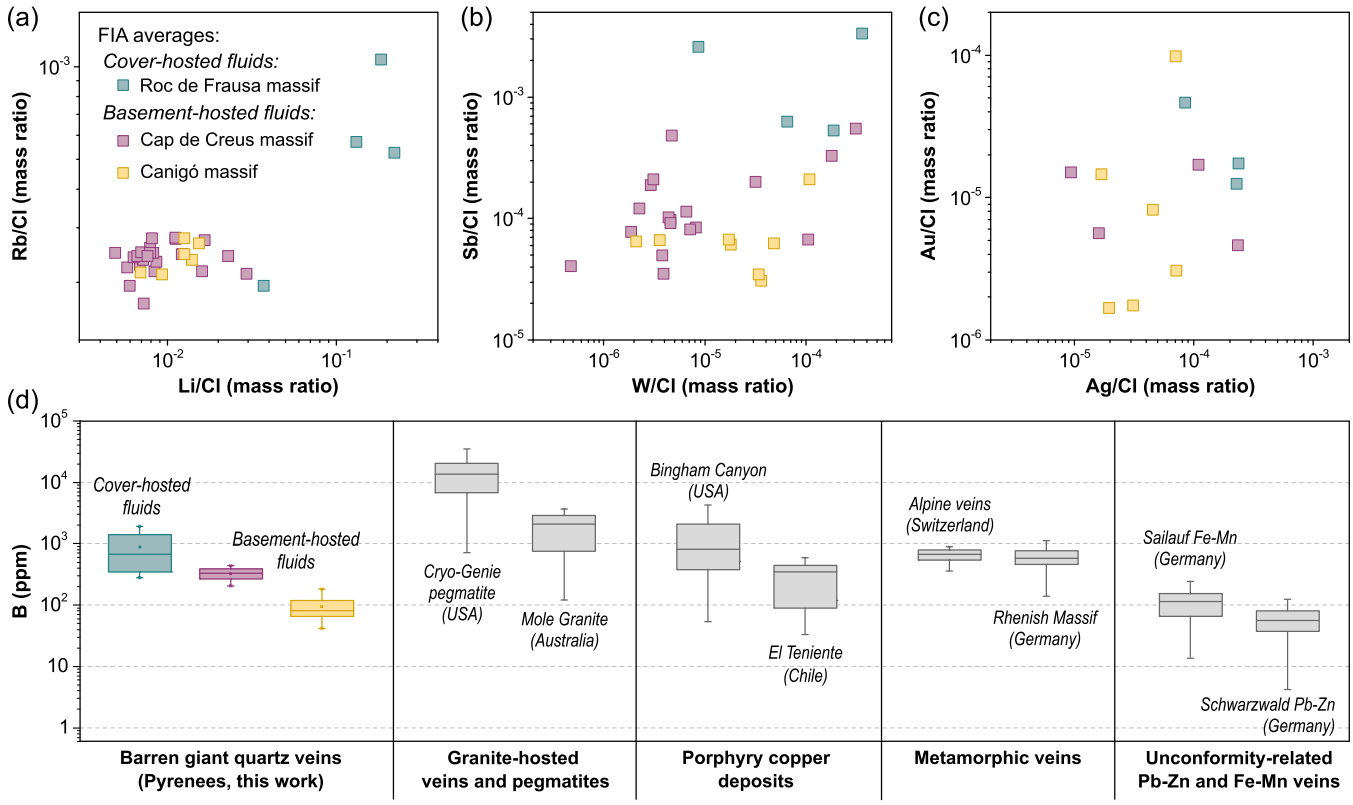

Fig. 15. Representative binary variation diagrams of Cl-normalised fluid inclusion assemblage (FIA) average element concentrations (mass ratios): (a) Alkali metals, Rb/Cl vs. Li/Cl; and ore metals, (b) Sb/Cl vs. W/Cl and (c) Au/Cl vs. Ag/Cl. (d) Boron concentrations in the basement- (Cap de Creus and Canigó massifs) and cover-hosted (Roc de Frausa massif) Type-2 quartz, and their comparison with reported Boron concentrations in magmatic, metamorphic, and sedimentary fluids from: Cryo-Genie pegmatite (Sirbescu et al., 2013), Mole granite (Audétat et al., 2000), Bingham Canyon (Landtwing et al., 2005, 2010), El Teniente (Klemm et al., 2007), Alpine quartz veins (Miron et al., 2013), Rhenish massif quartz veins (Marsala et al., 2013), Sailauf Fe-Mn veins (Fusswinkel et al., 2014), and Schwartzwald Pb-Zn veins (Fusswinkel et al., 2013); compilation after Wagner et al. (2016). Individual FIA averages of elemental concentrations and their corresponding 1σ standard deviations are provided Figs. 12 and 13 and in the Supplementary Material 1.

especially at the Cap de Creus GQVs (Fig. 11). This possibility will be discussed below within the Pyrenean setting.

Three FIAs from the Cap de Creus fluids (IDs #31, 9, and 19; Fig. 16) lie outside this compositional trend and define a cluster with significantly higher Br/Cl and moderate I/Cl ratios. These fluids show halogen ratios compatible with higher degrees of evaporation and resemble those of true basinal bittern brines (e.g., Richard et al., 2014; Yardley and Bodnar, 2014; Munoz et al., 2016). Petrographically, these FIAs are located in the outermost growth bands of two different samples. Therefore, they may be attributed to a more restricted, possibly late and more local circulation event of highly evolved residual evaporite fluids that previously underwent low degrees of organic matter interaction (Fig. 16b).

The halogen compositions of cover-hosted fluids are noteworthily different from those of the basement-hosted fluids (Fig. 16a). Cover-hosted fluids show I/Cl signatures similar to those that have most strongly interacted with organic matter at Cap de Creus and Canigó study areas, but significantly lower Br/Cl ratios. As these halogen signatures fall within the hypothetical seawater-organic matter interaction envelope shown in Fig. 16, they would also be compatible with variable degrees of organic matter interaction but involving a less strongly evaporated precursor fluid, compositionally closer to seawater. As this is the same process that is thought to control the tight compositional array found in metamorphic fluids (Böhlke and Irwin, 1992; Kendrick et al., 2001; Fusswinkel et al., 2022), the Roc de Frausa fluids are indistinguishable from metamorphic fluids on the basis of their halogen signatures alone. Furthermore, the fluids also partially overlap the halogen compositional range observed in magmatic-hydrothermal fluid systems from S-type granites (Lecumberri-Sanchez and Bodnar, 2018; Fusswinkel et al., 2022, and the references therof).

Fluids may reflect a source distinct to the location where they are presently found (Yardley, 2005). However, strong geological evidence suggest that, in the case of this study, the fluid source is not magmatic nor metamorphic. The cover rocks hosting the quartz veins were formed more than 200 Ma after the Variscan regional metamorphism and late-Variscan magmatism (Fig. 4) (González-Esvertit et al., 2022a), which are the youngest metamorphic and magmatic events recorded in the Eastern Pyrenees. There are no younger magmatic nor metamorphic events recorded in the Eastern Pyrenees that could represent a source for these fluids, and CO_2-rich fluid inclusions typical of metamorphic settings are conspicuously absent in the GQVs. The major element composition of these fluids also excludes magmatic sources, which generally produce Na–K–Fe-rich fluids such as those related to porphyry-forming brines (Bodnar et al., 2014). This is inferred because Fe does not show high concentrations typical of magmatic fluids and, overall, Na/Fe ratios are noteworthy lower (and Fe concentrations are thus higher; Fig. 14a) in cover-hosted fluids, where no magmatic host rocks are present, than in basement-hosted fluids, where host rocks are granitic rocks. Moreover, magmatic fluids typically have higher formation temperatures than those reported for either the studied GQVs (Fig. 10d-f) or other GQVs in the Pyrenees (Ayora and Casas, 1983; Ayora et al., 1984; Fonseca et al., 2015; González-Esvertit et al., 2024). Accordingly, the cover-hosted fluids at Roc de Frausa were not derived from magmatic or metamorphic sources at depth, and the most likely cause of the observed halogen signatures remains organic matter interaction with seawater-like precursor fluids that did not undergo

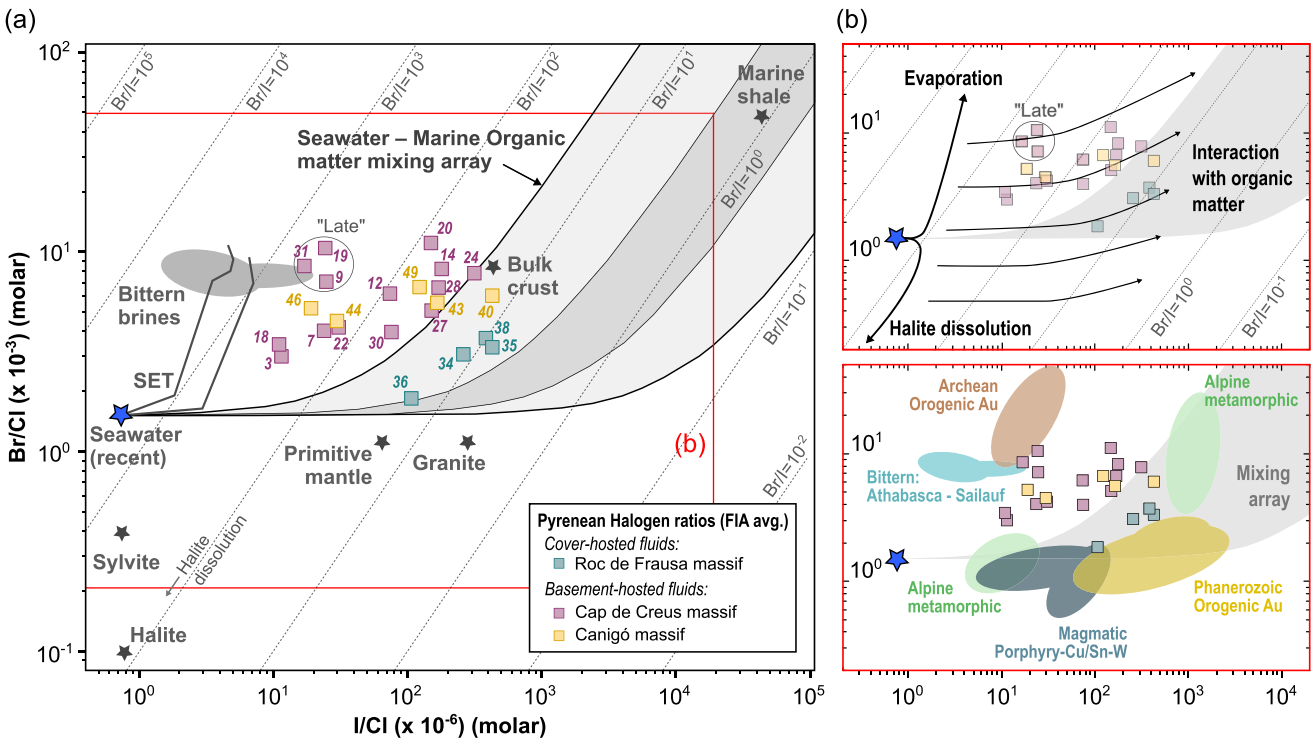

Fig. 16. (a) Halogen ratios of the investigated samples plotted together with halogen signatures of selected solid phases, the modern Seawater Evaporation Trajectory (SET), and the seawater-marine organic matter interaction mixing array inferred from marine pore fluids (light grey, Br/I = 0.5–23; dark grey, Br/I = 0.5–2.5); data labels are FIA IDs (see Figs. 12 and 13) (b) Potential Br/Cl and I/Cl halogen fractionation trajectories related to evaporation, halite dissolution, and interaction with organic matter (top), and data comparison with halogen signatures of crustal fluids known hitherto (bottom). Comparative diagrams in (b) after Fusswinkel et al. (2022). Since sedimentary pore waters evolve continuously into metamorphic pore fluids (Yardley, 1997; Yardley and Graham, 2002), all possible mixing proportions and halogen ratios of (Phanerozoic) metamorphic fluids plot within the grey mixing array envelope; but not all fluids within the grey envelope are necessarily metamorphic. Note that the data included for comparison in (b) is based on the (scarce) triple-halogen datasets that have been published hitherto; the true compositional variability of each crustal fluid type is likely much wider. See text for further discussion on why the halogen ratios plot should not be used as a fluid classification plot. Data sources: Krauskopf (1979), Fusswinkel et al. (2022), Scharrer et al. (2023) and the references therein.

significant evaporative halogen fractionation, which is also consistent with the lower salinities observed in the Roc de Frausa fluids and their CH_4(g) contents (Fig. 9d, Table 1). This non-magmatic origin for fluids that (apparently) show a magmatic halogen signature (Fig. 16b) highlights that the halogen ratios should not be used as a fluid classification tool, but rather for the qualitative assessment of the processes that operate during fluid evolution. Therefore, fluid source determination through the halogen ratios is not straightforward, and care must be taken when interpreting halogen data located in parts of the Cl-Br-I space where reference data overlap (Fig. 16).

5.2. *Fluid sources and evolution history in the Pyrenean setting*

The investigated basement- and cover-hosted fluids within the Type-2 GQV quartz show a wide range of features indicating that they were not released from metamorphic devolatilization reactions or magma reservoirs at depth. These include, among others, their moderate-high salinity values (Figs. 10, 11), the fluid systems inferred from microthermometry, and the triple-halogen ratios discussed above (cf. Klemm et al., 2007; Audétat et al., 2008; Seo et al., 2017; Fusswinkel et al., 2022). The stratigraphical and structural configuration of the study areas and the absence of metamorphic and magmatic events of similar age in the region further support this interpretation (Figs. 1–4). According to surface and subsurface data, metasedimentary basement rocks, Jurassic-Cretaceous carbonate successions, and the Eocene succession (evaporites, siltstones-marls, sandstones, and limestones) are the main rock units with which the fluids could have interacted (e.g., Carrillo et al., 2014; Tavani et al., 2018), whilst magmatic-metamorphic events are not recorded. Therefore, infiltration into the basement of surface or close-to surface fluids that underwent different degrees of evaporation (i.e., residual bittern brines) and fluid-rock interaction must be invoked as the initial chief processes in the evolution history of the investigated fluids.

The possible sources of these fluids may be attributed to Triassic or Eocene evaporation events that produced residual brines. Several evaporite horizons of these ages have widely been recognized in the Pyrenees, extensively cropping out and buried in the South-Central Pyrenees (Santolaria et al., 2017; Cofrade et al., 2023; Ramirez-Perez et al., 2023), but also in the subsurface of the South-Eastern Pyrenean basin (Serrat-1 and Vallfogona-1 wells; Ortí et al., 1987; Carrillo et al., 2014). However, the Triassic succession in the southern Roc de Frausa has been interpreted as a siliciclastic and carbonate sequence without presence of evaporite levels (Pujadas et al., 1989; Casas and Torrades, 2008). As halogen ratios indicating halite dissolution processes are not present in the investigated FIAs (Scharrer et al., 2023) (Fig. 16), this suggests that these fluids were sourced via the infiltration of residual evaporite brines into the basement, but prior to formation of later halite dissolution fluids in the sedimentary evaporite sequences. Salinity data (< 20 wt% $NaCl_{eq.}$; Fig. 12) suggest that these bittern brines were mixed with meteoric fluids at some stage, yielding to salinities below halite saturation but still retaining Br/Cl ratios typical of bittern brines (Kesler et al., 1996; Stoffell et al., 2008).

A noteworthy exception from the general compositional features are the Boron concentrations of the investigated fluids, which apparently are in disagreement with the aforementioned evidence that indicate a surface source. Generally, B in crustal fluids shows rather limited variations because it is commonly rock-buffered by minerals such as tourmaline or B-bearing muscovite and clay minerals (e.g., Wagner et al.,

2016). Processes such as dehydration of muscovite-bearing metasediments may produce a B enrichment in fluids released at depth and, therefore, the B content is often used to determine fluid sources (e.g., Sievers et al., 2017; Cheng et al., 2021). However, B concentrations within the analyzed FIAs (Fig. 15d) suggest that using this element as a fluid source proxy is not as straightforward as sometimes inferred. The B concentrations lie in a rather narrow range within each of the studied areas, although the full range of compositions overlap with values of magmatic and metamorphic fluids reported for different hydrothermal ore deposit types (Audétat et al., 2000; Landtwing et al., 2005, 2010; Klemm et al., 2007; Fusswinkel et al., 2013, 2014; Marsala et al., 2013; Miron et al., 2013; Sirbescu et al., 2013). Therefore, high or low B concentrations are not necessarily indicative of magmatic-hydrothermal or unconformity-related hydrothermal fluids, respectively (Fig. 15d).

During the infiltration to a certain depth into the basement of surface-derived fluids, metals such as Pb, Zn, and Cu may provide insights into fluid-rock interactions. These metals are typically transported as Cl-complexes and, therefore, medium to high salinity (chlorinity) and high temperature fluids often show high metal contents (Yardley, 2005). However, this does not apply to this case study, since the low-salinity fluids from the Roc de Frausa FIAs (Fig. 11) are those that show higher concentrations of Pb + Zn (Pb/Cl + Zn/Cl of ca. 10^{-2} in the cover vs. ca. 10^{-3} in the basement) and Cu (Cu/Cl of ca. 10^{-2} in the cover vs. ca. 10^{-3}–10^{-5} in the basement) (Fig. 14b, c), with T_h values similar to those of the other study areas (Fig. 10). This indicates that cover-hosted fluids have been circulating in the basement and that they have either infiltrated deeper and/or earlier than the basement-hosted fluids, in agreement with the aforementioned fluid stratification scenario, or may also reflect interaction with different rock types depending on the study area. Albeit not very high, base metal concentrations found in the studied FIAs are similar to other basinal systems, and noteworthy to some where basinal fluids originated MVT deposits (e.g., Fig. 6 in Stoffell et al., 2008). Pb and Zn concentrations are also similar to those found in Pb–Zn mineralization westwards the studied areas, in the Central Pyrenees (Cugerone et al., 2024). However, Mg concentrations were not detected during LA-ICP-MS measurements by these authors, which can be attributed to the absence of carbonate host rocks in the studied veins. Moreover, concentrations of most elements are also similar to other scenarios were basinal bittern brines infiltrate the basement (e.g., Scharrer et al., 2021). The observed halogen signatures that we obtained indeed indicate variable degrees of fluid-rock interaction (Fig. 16), which could have taken place within either the cover or the basement as suggested by high Mg (Figs. 13, 14d) and high Zn and Cu (Figs. 12, 13, 14b, c) concentrations, respectively. Organic matter abundantly present in carbonate successions within the cover rocks of the Southern Pyrenees (Puigdefàbregas et al., 1992; Carrillo et al., 2014), as well as in the low-grade metasedimentary basement rocks (Martín-Closas et al., 2018; Padel et al., 2018; Casas et al., 2019), may be responsible for the high I/Cl values observed in all three study areas. Fluid rock interaction with carbonate rocks may also be responsible for higher Mg contents in the Canigó and Roc de Frausa areas (Figs. 12, 13), where early Cambrian marble and Cretaceous limestone levels are present, respectively (Figs. 3, 4). One reasonable explanation for the cation concentrations and halogen ratios determined for the basement is a mixing process, since the intrinsic variations of I/Cl values are exceptionally large, with differences up to three orders of magnitude (Fig. 16). Since there is no possible scenario where fluids may migrate both upwards and downwards at the same time, unless a fluid sink at the mixing site is invoked (Bons et al., 2012, 2014), these settings would imply a basinal brine with a strong base metal leaching potential (e.g., Warren, 1996; Richard et al., 2016; Sośnicka et al., 2023) infiltrating deeper and/or first and then mixing, during ascent, with other fluids at shallower levels that have possibly infiltrated the crust at a later time.

Au concentrations measured in both basement- and cover-hosted fluids are also noteworthy (Fig. 12). They range from ca. 10^{-1} to 10 μg/g in both orogenic settings, although they have been found below the detection limit in some FIAs, mostly from the Cap de Creus massif. Some of the mechanisms originating gold-transporting fluids are crystallization of gold-rich shoshonitic lamprophyre magmas, devolatilization of felsic magmas, mantle fluids inducing granulite facies metamorphism, or devolatilization during prograde metamorphism (see a summary in Ridley and Diamond, 2000). However, as discussed above, magmatic or metamorphic fluid sources are unlikely for the investigated fluids based on their element concentrations, gas contents, halogen signatures, regional geologic setting, and relative age. One possible explanation for the obtained Au concentrations is the gold scavenging during fluid infiltration, which reinforces the idea that both cover- and basement-hosted fluids were infiltrated to significant depth. This agrees with some works relating surface-derived basinal fluids in gold transport and deposition in sediment-hosted 'orogenic' gold deposits (e.g. Large et al., 2009; Thomas et al., 2011). However, the fluid-rock interaction mechanisms, which perhaps involved gold-rich pyrite in the metasediments or areas with high gold concentrations present in the subsurface, as well as the relationship between Au contents and S concentration and speciation, remain unclear and may benefit from future studies.

The results obtained for the fluids investigated in this work show significant similarities and differences in terms of fluid properties, composition and sources when compared to fluid inclusion data reported for other GQVs elsewhere. Vein formation temperatures inferred from Th data (< 300 °C) agree with temperature constraints from chlorite thermometry obtained in other GQVs from the Pyrenees (González-Esvertit et al., 2024), but apparently clash with the classical assumption that these structures are formed by hot (300–450 °C) fluids (e.g., Kerrich and Feng, 1992; Tannock et al., 2020). Moreover, In the Central Alps (the Aar massif and Penninic nappes), Rauchenstein-Martinek et al. (2016) investigated the chemical evolution of fluids in the Alpine fissure veins and concluded that they record metamorphic fluids released during prograde devolatilization reactions. The fluids had interacted with organic matter or graphite after being trapped under rock-buffered conditions. Conversely, Rout et al. (2022) studied the 20 major *reefs* forming the "Bundelkhand giant quartz reef system" in Central India. They obtained a wide range in salinity (0–29 wt% $NaCl_{eqv}$) and Th (58–385 °C) values and, based on the composition of fluids and crystals trapped within the fluid inclusions, proposed mixing processes between meteoric and magmatic fluids. These contrasting fluid source interpretations responsible for GQV formation, coupled with the data reported here, suggest that the specific chemical constraints for the formation of GQVs still need to be fully constrained. Until fluid inclusion datasets similar to those reported here are made available for different GQV systems worldwide, the most reliable interpretation is that different scenarios of fluid origin and evolution may eventually lead to similar quartz accumulations within either basement or cover rocks, as long as there is an abundant source of silica, an efficient transport mechanism for mobilising that silica, and a sufficient time span for its transport and precipitation.

6. Concluding remarks

This study demonstrates that petrographically-constrained elemental concentration analysis of individual fluid inclusions, combined with the determination of fluid density, temperature, and salinity, represent a powerful approach for assessing the sources and evolution of fluids responsible for mineral reactions in the Earth's crust. Moreover, EBSD analysis may also help assessing the reliability of fluid inclusion data in sample areas with signs of post-entrapment modifications of fluid inclusions. Overall, such multi-method fluid inclusion studies often involve a progressive loss of data as different techniques are applied. These are often related to material loss during wafer cutting, inclusion decrepitation during microthermometric analysis, or out of control ablations resulting in fluid inclusion leakage or fragmentation. For example, the total number of fluid inclusion signals obtained from LA-ICP-MS microanalyses was 357, out of which 199 met the data quality

criteria (see Sub-section 3.6). Some of these reliable analyses have shown anomalous element concentrations when compared to the majority of FIA concentration averages, and would have averaged the fluid inclusion compositions resulting in "apparent" concentration values far from reality if bulk crush-leach analysis was performed in this work (e.g., Wilkinson, 2014; see a graphical example in Fig. 7 from Walter et al., 2018). Moreover, the progressive data loss during the multi-method approach implies that obtaining a reliable fluid inclusion signal was not possible for some FIAs that were already investigated through microthermometry and Raman micro-spectroscopy. This fact highlights the importance of preserving a detailed record of petrographic observations with workflows similar to the GIS-based petrography approach presented here, allowing a virtual revisit of samples following destructive analysis, as well as of using strict data quality constrains that ensure that the results, despite sometimes scarce or incomplete, are reliable.

Collisional mountain belts are exceptional natural laboratories for the comparative assessment of fluid-rock interaction recorded in fluids within the cover and the basement rocks. This study shows that fluids may reflect a source and evolution history that is distinct from that of their sampling location. Both basement- and cover-hosted fluids investigated were sourced from surface or near-surface environments and have subsequently infiltrated the continental crust to significant depths. However, their contrasting fluid compositions and evolution histories underscore the importance of considering both basement and cover environments when evaluating fluid systems in orogenic settings. Anomalous element concentrations in few specific FIAs further highlight the robustness of LA-ICP-MS microanalysis of individual fluid inclusions compared to bulk methods. The large variations of the Br/Cl, I/Cl, and Br/I ratios observed call for caution when using halogen ratios as proxies for fluid sources. The halogen data may allow a qualitative assessment of processes involving halogen fractionation during fluid evolution history rather than providing a straightforward fingerprint of the fluid origin.

Supplementary data to this article can be found online at https://doi.org/10.1016/j.chemgeo.2024.122578.

CRediT authorship contribution statement

Eloi González-Esvertit: Writing – original draft, Visualization, Software, Methodology, Investigation, Formal analysis, Data curation, Conceptualization. **Tobias Fusswinkel:** Writing – review & editing, Validation, Supervision, Methodology. **Àngels Canals:** Writing – review & editing, Supervision, Methodology, Investigation, Funding acquisition, Conceptualization. **Josep Maria Casas:** Writing – review & editing, Supervision, Methodology, Investigation, Funding acquisition, Conceptualization. **Joyce Neilson:** Writing – review & editing, Validation, Methodology, Funding acquisition. **Thomas Wagner:** Writing – review & editing, Validation, Methodology. **Enrique Gomez-Rivas:** Writing – review & editing, Supervision, Methodology, Investigation, Funding acquisition, Conceptualization.

Declaration of competing interest

The authors declare that they have no known competing financial interests or personal relationships that could have appeared to influence the work reported in this paper.

Acknowledgements

We thank Thomas Pettke and an anonymous reviewer for their insightful and constructive comments, which have greatly contributed to improving this paper, together with the editorial guidance of Marco Fiorentini. John Still is acknowledged for his help during SEM-EBSD data acquisition at the ACEMAC Facility (University of Aberdeen). We acknowledge Oxford Instruments for providing a Student Licence of the AZtecFlex software package. EGE acknowledges the funding provided by the Geological Society of London (GSL) Student Research Grants, the Fundació Universitaria Agustí Pedro i Pons, and the PhD grants funded by Generalitat de Catalunya and the European Social Fund (2021 FI_B 00165 and 2022 FI_B1 00043). TW acknowledges support from the German Research Foundation (DFG), infrastructure grant INST222/1401-1. EGR acknowledges funding provided by the Spanish Ministry of Science, Innovation and Universities ("Ramón y Cajal" fellowship RYC2018-026335-I, funded by MCIN/AEI/ /10.13039/501100011033/ESF). This work is a contribution to the Projects PID2021-122467NB-C22 and PID2021-125585NB-I00 (MCIN/AEI/FEDER-UE/10.13039/501100011033), PID2020-118999GB-I00 (MCIN/AEI/10.13039/501100011033), CNS2023-145382 (MCIN/AEI/10.13039/501100011033/EUNextGenerationEU/PRT) and to the Sedimentary Geology and Modelitzacio Geodinamica de la Litosfera Research Groups funded by AGAUR (2021 SGR 00349 and 2021 SGR 00410).

Data availability

Data is available in the Supplementary Materials

References

Aguilar, C., Liesa, M., Castiñeiras, P., Navidad, M., 2014. Late Variscan metamorphic and magmatic evolution in the eastern Pyrenees revealed by U–Pb age zircon dating. J. Geol. Soc. 171 (2), 181–192.

Allan, M.M., Yardley, B.W.D., Forbes, L.J., Shmulovich, K.I., Banks, D.A., Shepherd, T.J., 2005. Validation of LA-ICP-MS fluid inclusion analysis with synthetic fluid inclusions. Am. Mineral. 90, 1767–1775. https://doi.org/10.2138/am.2005.1822.

Audétat, A., Günther, D., Heinrich, C.A., 2000. Causes for Large-Scale Metal Zonation around Mineralized Plutons: Fluid Inclusion LA-ICP-MS evidence from the Mole Granite, Australia. Econ. Geol. 95, 1563–1581. https://doi.org/10.2113/gsecongeo.95.8.1563.

Audétat, A., Pettke, T., Heinrich, C.A., Bodnar, R.J., 2008. Special Paper: the Composition of Magmatic-Hydrothermal Fluids in Barren and Mineralized Intrusions. Econ. Geol. 103, 877–908. https://doi.org/10.2113/gsecongeo.103.5.877.

Ayora, C., Casas, J.M., 1983. Estudi microtermomètric dels filons de quars de les Esquerdes de Rojà, Massís de Canigó, Pirineu Oriental. Acta Geol. Hisp. 18, 35–46.

Ayora, C., Carreras, J., Casas, J.M., Liesa, M., 1984. Informe quarsos. Internal report of the University of Barcelona (Available Under Request). Universitat de Barcelona, Barcelona.

Bakker, R.J., 2003. Package FLUIDS 1. Computer programs for analysis of fluid inclusion data and for modelling bulk fluid properties. Chem. Geol. Eur. Curr. Res. Fluid Inclus. 194, 3–23. https://doi.org/10.1016/S0009-2541(02)00268-1.

Banks, D.A., Da Vies, G.R., Yardley, B.W.D., McCaig, A.M., Grant, N.T., 1991. The chemistry of brines from an Alpine thrust system in the Central Pyrenees: an application of fluid inclusion analysis to the study of fluid behaviour in orogenesis. Geochim. Cosmochim. Acta 55, 1021–1030. https://doi.org/10.1016/0016-7037(91)90160-7.

Berni, G.V., Wagner, T., Fusswinkel, T., 2020. From a F-rich granite to a NYF pegmatite: Magmatic-hydrothermal fluid evolution of the Kymi topaz granite stock. SE Finland. Lithos 364–365, 105538. https://doi.org/10.1016/j.lithos.2020.105538.

Bodnar, R., 2003. Reequilibration of fluid inclusions. Fluid inclusions: Analysis and Interpretation. Mineral. Assoc. Canada 32, 213–230.

Bodnar, R.J., Lecumberri-Sanchez, P., Moncada, D., Steele-MacInnis, M., 2014. Fluid Inclusions in Hydrothermal Ore Deposits. In: Treatise on Geochemistry. Elsevier, pp. 119–142. https://doi.org/10.1016/B978-0-08-095975-7.01105-0.

Böhlke, J.K., Irwin, J.J., 1992. Laser microprobe analyses of noble gas isotopes and halogens in fluid inclusions: analyses of microstandards and synthetic inclusions in quartz. Geochim. Cosmochim. Acta 56, 187–201. https://doi.org/10.1016/0016-7037(92)90126-4.

Bongiovanni, M., Fusswinkel, T., Marks, M.A.W., 2024. Unravelling the effects of magmatic fractionation, fluid phase separation and dilution on the composition of magmatic-hydrothermal fluids of the Cornubian Batholith (SW England). Chem. Geol. 122119. https://doi.org/10.1016/j.chemgeo.2024.122119.

Bonin, B., 1990. From orogenic to anorogenic settings: Evolution of granitoid suites after a major orogenesis. Geol. J. 25, 261–270. https://doi.org/10.1002/gj.3350250309.

Bons, P.D., Gomez-Rivas, E., 2013. Gravitational fractionation of isotopes and dissolved components as a first-order process in crustal fluids. Econ. Geol. 108, 1195–1201. https://doi.org/10.2113/econgeo.108.5.1195.

Bons, P.D., Gomez-Rivas, E., 2020. Origin of Meteoric Fluids in Extensional Detachments. Geofluids 2020, 1–8. https://doi.org/10.1155/2020/7201545.

Bons, P.D., Elburg, M.A., Gomez-Rivas, E., 2012. A review of the formation of tectonic veins and their microstructures. J. Struct. Geol. 43, 33–62. https://doi.org/10.1016/j.jsg.2012.07.005.

Bons, P.D., Fusswinkel, T., Gomez-Rivas, E., Markl, G., Wagner, T., Walter, B., 2014. Fluid mixing from below in unconformity-related hydrothermal ore deposits. Geology 42, 1035–1038. https://doi.org/10.1130/G35708.1.

Brown, M., 1995. P–T–t evolution of orogenic belts and the causes of regional metamorphism. Geol. Soc. Lond. Mem. 16, 67–81. https://doi.org/10.1144/GSL.MEM.1995.016.01.09.

Burbank, D.W., Vergés, J., Muñoz, J.A., Bentham, P., 1992. Coeval hindward- and forward-imbricating thrusting in the south-Central Pyrenees, Spain: timing and rates of shortening and deposition. GSA Bull. 104, 3–17. https://doi.org/10.1130/0016-7606(1992)104<0003:CHAFIT>2.3.CO;2.

Canals, A., Cardellach, E., Moritz, R., Soler, A., 1999. The influence of enclosing rock type on barite deposits, eastern Pyrenees, Spain: fluid inclusion and isotope (Sr, S, O, C) data. Mineral. Deposita 34, 199–210. https://doi.org/10.1007/s001260050196.

Cardellach, E., Ayora, C., Soler, A., Delgado, J., 1992. The origin of fluids involved in the formation of gold-bearing skarns of the Andorra granite (Central Pyrenees, Spain): Sulphur isotope data. Mineral. Petrol. 45, 181–193. https://doi.org/10.1007/BF01163111.

Carreras, J., 2001. Zooming on Northern Cap de Creus shear zones. J. Struct. Geol. 23, 1457–1486. https://doi.org/10.1016/S0191-8141(01)00011-6.

Carrillo, E., Rosell, L., Ortí, F., 2014. Multiepisodic evaporite sedimentation as an indicator of palaeogeographical evolution in foreland basins (South-eastern Pyrenean basin, Early-Middle Eocene). In: Eberli, G. (Ed.). Sedimentology 61, 2086–2112. https://doi.org/10.1111/sed.12140.

Casas, J.M., 1984. Estudi de la deformació en els gneis del massís del Canigó. PhD Thesis. Barcelona,. Universitat de Barcelona, p. 284. Unpublished.

Casas, J.M., 2010. Ordovician deformations in the Pyrenees: new insights into the significance of pre-Variscan ('sardic') tectonics. Geol. Mag. 147, 674–689. https://doi.org/10.1017/S0016756809990756.

Casas, J.M., Torrades, P., 2008. Estructura de la cuenca mesozoica de Els Banys d'Arles. Geotemas (Madrid) 685–688.

Casas, J.M., Castiñeiras, P., Navidad, M., Liesa, M., Carreras, J., 2010. New insights into the Late Ordovician magmatism in the Eastern Pyrenees: U–Pb SHRIMP zircon data from the Canigó massif. Gondwana Res. 17, 317–324. https://doi.org/10.1016/j.gr.2009.10.006.

Casas, J.M., Álvaro, J.J., Clausen, S., Padel, M., Puddu, C., Sanz-López, J., Sánchez-García, T., Navidad, M., Castiñeiras, P., Liesa, M., 2019. Palaeozoic Basement of the Pyrenees. In: Quesada, C., Oliveira, J.T. (Eds.), The Geology of Iberia: A Geodynamic Approach, Regional Geology Reviews. Springer International Publishing, Cham, pp. 229–259. https://doi.org/10.1007/978-3-030-10519-8_8.

Castiñeiras, P., Navidad, M., Liesa, M., Carreras, J., Casas, J.M., 2008. U–Pb zircon ages (SHRIMP) for Cadomian and Early Ordovician magmatism in the Eastern Pyrenees: New insights into the pre-Variscan evolution of the northern Gondwana margin. Tectonophysics, The Foundations and Birth of the Rheic Ocean: Avalonian−Cadomian Orogenic Processes and Early Palaeozoic Rifting at the Northern Gondwana Margin / Evolution and Closure of the Rheic Ocean: Palaeozoic Drift of Peri-Gondwanan Terranes and Alleghenian−Variscan Orogenic Processes, 461, pp. 228–239. https://doi.org/10.1016/j.tecto.2008.04.005.

Cathelineau, M., Boiron, M.-C., Fourcade, S., Ruffet, G., Clauer, N., Belcourt, O., Coulibaly, Y., Banks, D.A., Guillocheau, F., 2012. A major Late Jurassic fluid event at the basin/basement unconformity in western France: 40Ar/39Ar and K–Ar dating, fluid chemistry, and related geodynamic context. Chem. Geol. 322–323, 99–120. https://doi.org/10.1016/j.chemgeo.2012.06.008.

Cheng, L., Zhang, C., Liu, X., Yang, X., Zhou, Y., Horn, I., Weyer, S., Holtz, F., 2021. Significant boron isotopic fractionation in the magmatic evolution of Himalayan leucogranite recorded in multiple generations of tourmaline. Chem. Geol. 571, 120194. https://doi.org/10.1016/j.chemgeo.2021.120194.

Cirés, J., Morales, V., Liesa, M., Carreras, J., Escuer, J., Pujadas, J., 1994. Mapa Geológico y Memoria de la Hoja nº 220 (La Jonquera). Mapa Geológico de España E. 1:200.000 IGME.

Cofrade, G., Závada, P., Kŕýza, O., Cantarero, I., Gratacós, Ò., Ferrer, O., Adineh, S., Ramirez-Perez, P., Roca, E., Travé, A., 2023. The kinematics of a salt sheet recorded in an array of distorted intrasalt stringers (Les Avellanes Diapir – South-Central Pyrenees). J. Struct. Geol. 176, 104963. https://doi.org/10.1016/j.jsg.2023.104963.

Cox, S.F., 2005. Coupling between Deformation, Fluid Pressures, and Fluid Flow in Ore-Producing Hydrothermal Systems at Depth in the Crust. One Hundredth Anniversary Volume. Soc. Econom. Geol. https://doi.org/10.5382/AV100.04.

Cruset, D., Vergés, J., Muñoz-López, D., Moragas, M., Cantarero, I., Travé, A., 2023. Fluid evolution from extension to compression in the Pyrenean Fold Belt and Basque-Cantabrian Basin: a review. Earth Sci. Rev. 243, 104494. https://doi.org/10.1016/j.earscirev.2023.104494.

Cugerone, A., Salvi, S., Kouzmanov, K., Laurent, O., Cenki, B., 2024. Tracing fluid signature and metal mobility in complex orogens: insights from Pb-Zn mineralization in the Pyrenean Axial Zone. Miner. Deposita 1–23.

de Riese, T., Bons, P.D., Gomez-Rivas, E., Sachau, T., 2020. Interaction between Crustal-Scale Darcy and Hydrofracture Fluid Transport: a Numerical Study. In: Manning, a. H. (Ed.). Geofluids 2020, 1–14. https://doi.org/10.1155/2020/8891801.

DeCelles, P.G., Giles, K.A., 1996. Foreland basin systems. Basin Res. 8, 105–123. https://doi.org/10.1046/j.1365-2117.1996.01491.x.

Delgado, J., Soler, A., 2010. Ilvaite stability in skarns from the northern contact of the Maladeta batholith, Central Pyrenees (Spain). Eur. J. Mineral. 22, 363–380. https://doi.org/10.1127/0935-1221/2010/0022-2021.

Diamond, L.W., 1990. Fluid inclusion evidence for P-V-T-X evolution of hydrothermal solutions in late-Alpine gold-quartz veins at Brusson, Val d'Ayas, Northwest Italian Alps. Am. J. Sci. 290, 912–958. https://doi.org/10.2475/ajs.290.8.912.

Druguet, E., 1997. The Structure of the NE Cap de Creus Peninsula Relationships with Metamorphism and Magmatism. PhD Thesis. Barcelona,. Universitat Autònoma de Barcelona. Unpublished.

Druguet, E., Carreras, J., 2019. Folds and Shear zones at Cap de Creus. In: Field Trip Guide XXXI Reunión de La Comisión de Tectónica - SGE 27.

Druguet, E., Castro, A., Chichorro, M., Pereira, M.F., Fernández, C., 2014. Zircon geochronology of intrusive rocks from Cap de Creus, Eastern Pyrenees. Geol. Mag. 151, 1095–1114. https://doi.org/10.1017/S0016756814000041.

Fonseca, H.A.M., Canals i Sabaté, À., Cires, J., Casas Tuset, J.M., 2015. The Roses giant quartz vein (Cap de Creus, Eastern Pyrenees): Geology and fluid inclusion data. In: Articles Publicats En Revistes (Mineralogia, Petrologia i Geologia Aplicada).

Ford, M., Vergés, J., 2021. Evolution of a salt-rich transtensional rifted margin, eastern North Pyrenees, France. J. Geol. Soc. Lond. 178. https://doi.org/10.1144/jgs2019-157 jgs2019-157.

Fu, B., Kendrick, M.A., Fairmaid, A.M., Phillips, D., Wilson, C.J.L., Mernagh, T.P., 2012. New constraints on fluid sources in orogenic gold deposits, Victoria, Australia. Contrib. Mineral. Petrol. 163, 427–447. https://doi.org/10.1007/s00410-011-0678-4.

Fusswinkel, T., Wagner, T., Wälle, M., Wenzel, T., Heinrich, C.A., Markl, G., 2013. Fluid mixing forms basement-hosted Pb-Zn deposits: Insight from metal and halogen geochemistry of individual fluid inclusions. Geology 41, 679–682. https://doi.org/10.1130/G34092.1.

Fusswinkel, T., Wagner, T., Wenzel, T., Wälle, M., Lorenz, J., 2014. Red bed and basement sourced fluids recorded in hydrothermal Mn–Fe–as veins, Sailauf (Germany): a LA-ICPMS fluid inclusion study. Chem. Geol. 363, 22–39. https://doi.org/10.1016/j.chemgeo.2013.10.026.

Fusswinkel, T., Wagner, T., Sakellaris, G., 2017. Fluid evolution of the Neoarchean Pampalo orogenic gold deposit (E Finland): Constraints from LA-ICPMS fluid inclusion microanalysis. Chem. Geol. 450, 96–121. https://doi.org/10.1016/j.chemgeo.2016.12.022.

Fusswinkel, T., Giehl, C., Beermann, O., Fredriksson, J.R., Garbe-Schönberg, D., Scholten, L., Wagner, T., 2018. Combined LA-ICP-MS microanalysis of iodine, bromine and chlorine in fluid inclusions. J. Anal. At. Spectrom. 33, 768–783. https://doi.org/10.1039/C7JA00415J.

Fusswinkel, T., Niinikoski-Fusswinkel, P., Wagner, T., 2022. Halogen ratios in crustal fluids through time—Proxies for the emergence of aerobic life? Geology 50, 1096–1100. https://doi.org/10.1130/G50182.1.

Gleeson, S.A., Yardley, B.W.D., Boyce, A.J., Fallick, A.E., Munz, I.-A., 2000. From basin to basement: the movement of surface fluids into the crust. J. Geochem. Explor. 69–70, 527–531. https://doi.org/10.1016/S0375-6742(00)00114-X.

Goldfarb, R.J., Groves, D.I., 2015. Orogenic gold: Common or evolving fluid and metal sources through time. Lithos, Geochemi. Earth Syst. – A 233, 2–26. https://doi.org/10.1016/j.lithos.2015.07.011. Special Issue in Memory of Robert Kerrich.

Goldfarb, R.J., Groves, D.I., Gardoll, S., 2001. Orogenic gold and geologic time: a global synthesis. Ore Geol. Rev. 18, 1–75. https://doi.org/10.1016/S0169-1368(01)00016-6.

Goldstein, R.H., 2001. Fluid inclusions in sedimentary and diagenetic systems. Lithos, Fluid Inclusions: phase Relationships - Methods - applications. A Spe. Iss. Honour Jacqu. Touret 55, 159–193. https://doi.org/10.1016/S0024-4937(00)00044-X.

Goldstein, R.H., Reynolds, T.J., 1994. Systematics of fluid inclusions in diagenetic minerals. SEPM Short Course 31, 199.

González-Esvertit, E., Canals, À., Casas, J.M., Nieto, F., 2020. Insights into the structural evolution of the pre-Variscan rocks of the Eastern Pyrenees from La Molina quartz veins; constraints on chlorite and fluid inclusion thermometry. Geol. Acta 18. https://doi.org/10.1344/GeologicaActa2020.18.18, 1–XXIV.

González-Esvertit, E., Canals, À., Bons, P.D., Casas, J.M., Gomez-Rivas, E., 2022a. Compiling regional structures in geological databases: the giant quartz veins of the Pyrenees as a case study. J. Struct. Geol. 163, 104705. https://doi.org/10.1016/j.jsg.2022.104705.

González-Esvertit, E., Canals, À., Bons, P.D., Murta, H., Casas, J.M., Gomez-Rivas, E., 2022b. Geology of giant quartz veins and their host rocks from the Eastern Pyrenees (Southwest Europe). J. Maps 19, 1–13. https://doi.org/10.1080/17445647.2022.2133642.

González-Esvertit, E., Alcalde, J., Gomez-Rivas, E., 2023. IESDB – the Iberian Evaporite Structure Database. Earth Syst. Sci. Data 15, 3131–3145. https://doi.org/10.5194/essd-15-3131-2023.

González-Esvertit, E., Canals, A., Bons, P.D., Casas, J.M., Nieto, F., Gomez-Rivas, E., 2024. Chlorite chemical refinement during giant quartz vein formation. GSA Bull. https://doi.org/10.1130/B37510.1.

González-Esvertit, E., Prieto-Torrell, C., Bons, P.D., Canals, À., Casas, J.M., Elburg, M.A., Gomez-Rivas, E., 2025. A review of the granite concept through time. Earth Sci. Rev. 105008. https://doi.org/10.1016/j.earscirev.2024.105008.

Guillong, M., Pettke, T., 2012. Depth dependent element ratios in fluid inclusion analysis by laser ablation ICP-MS. J. Anal. At. Spectrom. 27, 505–508. https://doi.org/10.1039/C2JA10147E.

Guillong, M., Meier, D.L., Allan, M.M., Heinrich, C.A., Yardley, B.W., 2008. Appendix A6: SILLS: a MATLAB-based program for the reduction of laser ablation ICP-MS data of homogeneous materials and inclusions. Mineral. Assoc. Canada Short Course 40, 328–333.

Guitard, G., 1965. Carte Géologique des Massifs du Canigou et de la Carançà à 1/50.000. BRGM Service de la Carte Géologique de France..

Guitard, G., 1970. Le métamorphisme hercynien mésozonal et les gneiss oeillés du massif du Canigou (Pyrénées orientales). Mémoir. Du Bureau de Recherch. Géolog. et Minières (BRGM) 63, 353.

Heinrich, C.A., Pettke, T., Halter, W.E., Aigner-Torres, M., Audétat, A., Günther, D., Hattendorf, B., Bleiner, D., Guillong, M., Horn, I., 2003. Quantitative multi-element analysis of minerals, fluid and melt inclusions by laser-ablation inductively-coupled-plasma mass-spectrometry. Geochim. Cosmochim. Acta 67, 3473–3497.

Jochum, K.P., Weis, U., Stoll, B., Kuzmin, D., Yang, Q., Raczek, I., Jacob, D.E., Stracke, A., Birbaum, K., Frick, D.A., Günther, D., Enzweiler, J., 2011. Determination of Reference Values for NIST SRM 610–617 Glasses following ISO guidelines.

Geostand. Geoanal. Res. 35, 397–429. https://doi.org/10.1111/j.1751-908X.2011.00120.x.
Kendrick, M.A., 2012. High precision Cl, Br and I determinations in mineral standards using the noble gas method. Chem. Geol. 292, 116–126.
Kendrick, M.A., 2018. Halogens in Seawater, Marine Sediments and the Altered Oceanic Lithosphere. In: Harlov, D.E., Aranovich, L. (Eds.), The Role of Halogens in Terrestrial and Extraterrestrial Geochemical Processes: Surface, Crust, and Mantle, Springer Geochemistry. Springer International Publishing, Cham, pp. 591–648. https://doi.org/10.1007/978-3-319-61667-4_9.
Kendrick, M.A., Burgess, R., Pattrick, R.A.D., Turner, G., 2001. Halogen and Ar–Ar age determinations of inclusions within quartz veins from porphyry copper deposits using complementary noble gas extraction techniques. Chem. Geol. 177, 351–370. https://doi.org/10.1016/S0009-2541(00)00419-8.
Kendrick, M.A., Burgess, R., Harrison, D., Bjørlykke, A., 2005. Noble gas and halogen evidence for the origin of Scandinavian sandstone-hosted Pb-Zn deposits. Geochim. Cosmochim. Acta 69, 109–129. https://doi.org/10.1016/j.gca.2004.05.045.
Kerrich, R., Feng, R., 1992. Archean geodynamics and the Abitibi-Pontiac collision: implications for advection of fluids at transpressive collisional boundaries and the origin of giant quartz vein systems. Earth Sci. Rev. 32, 33–60. https://doi.org/10.1016/0012-8252(92)90011-H.
Kesler, S.E., Martini, A.M., Appold, M.S., Walter, L.M., 1996. Na-Cl-Br systematics of fluid inclusions from Mississippi Valley-type deposits, Appalachian Basin: Constraints on solute origin and migration paths. Geochim. Cosmochim. Acta 60 (2), 225–233.
Klemm, L., Pettke, T., Graeser, S., Mullis, J., Kouzmanov, K., 2004. Fluid mixing as the cause of sulphide precipitation at Albrunpass, Binn Valley, Central Alps. Swiss Bull. Mineral. Petrol. 84 (1), 189–212.
Klemm, L.M., Pettke, T., Heinrich, C.A., Campos, E., 2007. Hydrothermal Evolution of the El Teniente Deposit, Chile: Porphyry Cu-Mo Ore Deposition from Low-Salinity Magmatic Fluids. Econ. Geol. 102, 1021–1045. https://doi.org/10.2113/gsecongeo.102.6.1021.
Koons, P.O., Craw, D., 1991. Evolution of fluid driving forces and composition within collisional orogens. Geophys. Res. Lett. 18, 935–938. https://doi.org/10.1029/91GL00910.
Krauskopf, K.B., 1979. Introduction to Geochemistry, 2nd edition. McGraw Hill, New York, p. 617.
Lacroix, B., Travé, A., Buatier, M., Labaume, P., Vennemann, T., Dubois, M., 2014. Syntectonic fluid-flow along thrust faults: example of the South-Pyrenean fold-and-thrust belt. Mar. Pet. Geol. 49, 84–98. https://doi.org/10.1016/j.marpetgeo.2013.09.005.
Lacroix, B., Baumgartner, L.P., Bouvier, A.-S., Kempton, P.D., Vennemann, T., 2018. Multi fluid-flow record during episodic mode I opening: a microstructural and SIMS study (Cotiella Thrust Fault, Pyrenees). Earth Planet. Sci. Lett. 503, 37–46. https://doi.org/10.1016/j.epsl.2018.09.016.
Landtwing, M.R., Pettke, T., Halter, W.E., Heinrich, C.A., Redmond, P.B., Einaudi, M.T., Kunze, K., 2005. Copper deposition during quartz dissolution by cooling magmatic–hydrothermal fluids: the Bingham porphyry. Earth Planet. Sci. Lett. 235, 229–243. https://doi.org/10.1016/j.epsl.2005.02.046.
Landtwing, M.R., Furrer, C., Redmond, P.B., Pettke, T., Guillong, M., Heinrich, C.A., 2010. The Bingham Canyon Porphyry Cu-Mo-au Deposit. III. Zoned Copper-Gold Ore Deposition by Magmatic Vapor expansion °. Econ. Geol. 105, 91–118. https://doi.org/10.2113/gsecongeo.105.1.91.
Large, R.R., Danyushevsky, L., Hollit, C., Maslennikov, V., Meffre, S., Gilbert, S., Bull, S., Scott, R., Emsbo, P., Thomas, H., Singh, B., Foster, J., 2009. Gold and trace element zonation in pyrite using a laser imaging technique: implications for the timing of gold in orogenic and carlin-style sediment-hosted deposits. Econ. Geol. 104, 635–668.
Laumonier, B., Calvet, M., Bayon, B.L., Barbey, P., 2015. Notice explicative de la feuille Prats-de-Mollo-La-Preste à 1/50,000. BRGM Éditions-Serv. Géol. Nation. 193.
Lecumberri-Sanchez, P., Bodnar, R.J., 2018. Halogen Geochemistry of Ore deposits: Contributions Towards Understanding sources and Processes. In: Harlov, D.E., Aranovich, L. (Eds.), The Role of Halogens in Terrestrial and Extraterrestrial Geochemical Processes: Surface, Crust, and Mantle. Springer International Publishing, Cham, pp. 261–305. https://doi.org/10.1007/978-3-319-61667-4_5.
Liesa, M., 1988. El metamorfisme del vessant sud del Massís del Roc de Frausa (Pirineus Orientals). PhD Thesis. Barcelona,. Universitat de Barcelona, Unpublished, p. 288.
Liesa, M., Aguilar, C., Castro, A., Gisbert, G., Reche, J., Muñoz, J.A., Vilà, M., 2021. The role of mantle and crust in the generation of calc-alkaline Variscan magmatism and its tectonic setting in the Eastern Pyrenees. Lithos 406–407, 106541. https://doi.org/10.1016/j.lithos.2021.106541.
Llorens, M.-G., Bons, P.D., Griera, A., Gomez-Rivas, E., 2013. When do folds unfold during progressive shear? Geology 41, 563–566. https://doi.org/10.1130/G33973.1.
MacKenzie, D.J., Craw, D., Mortensen, J., 2008. Structural controls on orogenic gold mineralisation in the Klondike goldfield, Canada. Mineral. Deposita 43, 435–448. https://doi.org/10.1007/s00126-007-0173-z.
Marsala, A., Wagner, T., 2016. Mass transfer and fluid evolution in late-metamorphic veins, Rhenish Massif (Germany): insight from alteration geochemistry and fluid-mineral equilibria modeling. Mineral. Petrol. 110, 515–545. https://doi.org/10.1007/s00710-016-0424-8.
Marsala, A., Wagner, T., Wälle, M., 2013. Late-metamorphic veins record deep ingression of meteoric water: a LA-ICPMS fluid inclusion study from the fold-and-thrust belt of the Rhenish Massif, Germany. Chem. Geol. 351, 134–153. https://doi.org/10.1016/j.chemgeo.2013.05.008.
Martín-Closas, C., Trias, S., Casas, J.M., 2018. New palaeobotanical data from Carboniferous Culm deposits constrain the age of the Variscan deformation in the eastern Pyrenees. Geol. Acta 16, 107–123. https://doi.org/10.1344/GeologicaActa2018.16.2.1.
McCaig, A.M., Wickham, S.M., Taylor, H.P., 1990. Deep fluid circulation in alpine shear zones, Pyrenees, France: field and oxygen isotope studies. Contrib. Mineral. Petrol. 106, 41–60. https://doi.org/10.1007/BF00306407.
McCaig, Andrew M., Tritlla, J., Banks, D.A., 2000. Fluid mixing and recycling during Pyrenean thrusting: evidence from fluid inclusion halogen ratios. Geochim. Cosmochim. Acta 64, 3395–3412. https://doi.org/10.1016/S0016-7037(00)00437-3.
Miron, G.D., Wagner, T., Wälle, M., Heinrich, C.A., 2013. Major and trace-element composition and pressure–temperature evolution of rock-buffered fluids in low-grade accretionary-wedge metasediments, Central Alps. Contrib. Mineral. Petrol. 165, 981–1008. https://doi.org/10.1007/s00410-012-0844-3.
Mullis, J., Dubessy, J., Poty, B., O'Neil, J., 1994. Fluid regimes during late stages of a continental collision: Physical, chemical, and stable isotope measurements of fluid inclusions in fissure quartz from a geotraverse through the Central Alps, Switzerland. Geochim. Cosmochim. Acta 58, 2239–2267. https://doi.org/10.1016/0016-7037(94)90008-6.
Muñoz, J.A., 1992. Evolution of a continental collision belt: ECORS-Pyrenees crustal balanced cross-section. In: McClay, K.R. (Ed.), Thrust Tectonics. Springer, Netherlands, Dordrecht, pp. 235–246. https://doi.org/10.1007/978-94-011-3066-0_21.
Muñoz, J.-A., Beamud, E., Fernández, O., Arbués, P., Dinarès-Turell, J., Poblet, J., 2013. The Ainsa Fold and thrust oblique zone of the Central Pyrenees: Kinematics of a curved contractional system from paleomagnetic and structural data: paleomagnetism in s pyrenees. Tectonics 32, 1142–1175. https://doi.org/10.1002/tect.20070.
Munoz, M., Baron, S., Boucher, A., Béziat, D., Salvi, S., 2016. Mesozoic vein-type Pb–Zn mineralization in the Pyrenees: Lead isotopic and fluid inclusion evidence from the Les Argentières and Lacore deposits. Comptes Rendus Geosci. Rifting Mountain Build. Pyrenean Belt 348, 322–332. https://doi.org/10.1016/j.crte.2015.07.001.
Muñoz, J.A., Mencos, J., Roca, E., Carrera, N., Gratacós, O., Ferrer, O., Fernández, O., 2018. The structure of the South-Central-Pyrenean fold and thrust belt as constrained by subsurface data. Geol. Acta 22.
Muñoz-López, D., Alías, G., Cruset, D., Cantarero, I., John, C.M., Travé, A., 2020. Influence of basement rocks on fluid evolution during multiphase deformation: the example of the Estamariu thrust in the Pyrenean Axial Zone. Solid Earth 11, 2257–2281. https://doi.org/10.5194/se-11-2257-2020.
Muñoz-López, D., Cruset, D., Vergés, J., Cantarero, I., Benedicto, A., Mangenot, X., Albert, R., Gerdes, A., Beranoaguirre, A., Travé, A., 2022. Spatio-temporal variation of fluid flow behavior along a fold: The Bóixols-Sant Corneli anticline (Southern Pyrenees) from U–Pb dating and structural, petrographic and geochemical constraints. Mar. Pet. Geol. 143, 105788. https://doi.org/10.1016/j.marpetgeo.2022.105788.
Naden, J., 1996. CalcicBrine: A Microsoft Excel 5.0 Add-in for Calculating Salinities from Microthermometric Data in the System NaCl-CaCl2-H2O. PACROFI VI, Madison, USA, pp. 97–98.
Nardini, N., Muñoz-López, D., Cruset, D., Cantarero, I., Martín-Martín, J.D., Benedicto, A., Gomez-Rivas, E., John, C.M., Travé, A., 2019. From early Contraction to Post-Folding Fluid Evolution in the Frontal part of the Bóixols Thrust Sheet (Southern Pyrenees) as Revealed by the Texture and Geochemistry of Calcite Cements. Minerals 9, 117. https://doi.org/10.3390/min9020117.
Navidad, M., Castiñeiras, P., Casas, J.M., Liesa, M., Belousova, E., Proenza, J., Aiglsperger, T., 2018. Ordovician magmatism in the Eastern Pyrenees: Implications for the geodynamic evolution of northern Gondwana. Lithos 314–315, 479–496. https://doi.org/10.1016/j.lithos.2018.06.019.
Ortí, F., Busquets, P., Rosell, L., Taberner, C., Utrilla, R., Quadras, M., 1987. La fase evaporítica del Eoceno medio (Luteciense) en la Cuenca Surpirenaica Catalana. Nuevas aportaciones. Rev. Del Instituto De Investigac. Geol. 44, 281–302.
Padel, M., Clausen, S., Álvaro, J.J., Casas, J.M., 2018. Review of the Ediacaran-lower Ordovician (pre-Sardic) stratigraphic framework of the Eastern Pyrenees, southwestern Europe. Geol. Acta 16, 339–365.
Pettke, T., 2008. Analytical protocols for element concentration and isotope ratio measurements in fluid inclusions by LA-(MC)-ICP-MS. In: Sylvester, P. (Ed.), Laser Ablation ICP-MS in the Earth Sciences: Current Practices and Outstanding Issues, 40. Mineral. Assoc. Can. Short Course Series, pp. 189–218.
Pettke, T., Oberli, F., Heinrich, C.A., 2010. The magma and metal source of giant porphyry-type ore deposits, based on lead isotope microanalysis of individual fluid inclusions. Earth Planet. Sci. Lett. 296, 267–277. https://doi.org/10.1016/j.epsl.2010.05.007.
Pettke, T., Oberli, F., Audétat, A., Guillong, M., Simon, A.C., Hanley, J.J., Klemm, L.M., 2012. Recent developments in element concentration and isotope ratio analysis of individual fluid inclusions by laser ablation single and multiple collector ICP-MS. Ore Geol. Rev. 44, 10–38. https://doi.org/10.1016/j.oregeorev.2011.11.001.
Pirajno, F., 2018. Halogens in Hydrothermal Fluids and their Role in the Formation and Evolution of Hydrothermal Mineral Systems. In: Harlov, D.E., Aranovich, L. (Eds.), The Role of Halogens in Terrestrial and Extraterrestrial Geochemical Processes: Surface, Crust, and Mantle. Springer Geochemistry. Springer International Publishing, Cham, pp. 759–804. https://doi.org/10.1007/978-3-319-61667-4_12.
Puigdefàbregas, C., Muñoz, J.A., Vergés, J., 1992. Thrusting and foreland basin evolution in the Southern Pyrenees. In: McClay, K.R. (Ed.), Thrust Tectonics. Springer, Netherlands, Dordrecht, pp. 247–254. https://doi.org/10.1007/978-94-011-3066-0_22.
Pujadas, J., Maria Casas, J., Anton Muñoz, J., Sabat, F., 1989. Thrust tectonics and paleogene syntectonic sedimentation in the Empordà area, southeastern Pyrenees. Geodin. Acta 3, 195–206. https://doi.org/10.1080/09853111.1989.11105186.

Quesnel, B., Boiron, M.-C., Cathelineau, M., Truche, L., Rigaudier, T., Bardoux, G., Agrinier, P., de Saint Blanquat, M., Masini, E., Gaucher, E.C., 2019. Nature and Origin of Mineralizing Fluids in Hyperextensional Systems: the Case of cretaceous Mg Metasomatism in the Pyrenees. Geofluids 2019, e7213050. https://doi.org/10.1155/2019/7213050.

Ramirez-Perez, P., Cantarero, I., Cofrade, G., Muñoz-López, D., Cruset, D., Sizun, J.-P., Travé, A., 2023. Petrological, petrophysical and petrothermal study of a folded sedimentary succession: the Oliana anticline (Southern Pyrenees), outcrop analogue of a geothermal reservoir. Glob. Planet. Chang. 222, 104057. https://doi.org/10.1016/j.gloplacha.2023.104057.

Rauchenstein-Martinek, K., Wagner, T., Wälle, M., Heinrich, C.A., Arlt, T., 2016. Chemical evolution of metamorphic fluids in the Central Alps, Switzerland: insight from LA-ICPMS analysis of fluid inclusions. Geofluids 16, 877–908. https://doi.org/10.1111/gfl.12194.

Richard, A., Kendrick, M.A., Cathelineau, M., 2014. Noble gases (Ar, Kr, Xe) and halogens (Cl, Br, I) in fluid inclusions from the Athabasca Basin (Canada): Implications for unconformity-related U deposits. Precambrian Res. 247, 110–125. https://doi.org/10.1016/j.precamres.2014.03.020.

Kendrick, M.A., Burnard, P., 2013. Noble gases and halogens in fluid inclusions: a journey through the Earth's crust. The Noble Gases as Geochemical Tracers, pp. 319–369.

Richard, A., Cathelineau, M., Boiron, M.-C., Mercadier, J., Banks, D.A., Cuney, M., 2016. Metal-rich fluid inclusions provide new insights into unconformity-related U deposits (Athabasca Basin and Basement, Canada). Mineral. Deposita 51, 249–270. https://doi.org/10.1007/s00126-015-0601-4.

Ridley, J.R., Diamond, L.W., 2000. Fluid chemistry of orogenic lode gold deposits and implications for genetic models. In: Hagemann, S.G., Brown, P.E. (Eds.), Gold in 2000. Society of Economic Geologists, p. 0. https://doi.org/10.5382/Rev.13.04.

Roedder, E., 1984. Fluid Inclusions. De Gruyter. https://doi.org/10.1515/9781501508271.

Rout, D., Panigrahi, M.K., Mernagh, T.P., Pati, J.K., 2022. Origin of the Paleoproterozoic "Giant Quartz Reef" System in the Bundelkhand Craton, India: Constraints from Fluid Inclusion Microthermometry, Raman Spectroscopy, and Geochemical Modelling. Lithosphere 2022, 3899542. https://doi.org/10.2113/2022/3899542.

Santanach, P., 1972. Sobre una discordancia en el Paleozoico inferior de los Pirineos orientales. Acta Geol. Hisp. 7, 129–132.

Scharrer, M., Reich, R., Fusswinkel, T., Walter, B.F., Markl, G., 2021. Basement aquifer evolution and the formation of unconformity-related hydrothermal vein deposits: LA-ICP-MS analyses of single fluid inclusions in fluorite from SW Germany. Chem. Geol. 575, 120260. https://doi.org/10.1016/j.chemgeo.2021.120260.

Santolaria, P., Casas-Sainz, A.M., Soto, R., Casas, A., 2017. Gravity modelling to assess salt tectonics in the western end of the South Pyrenean Central Unit. J. Geol. Soc. 174 (2), 269–288.

Scharrer, M., Fusswinkel, T., Markl, G., 2023. Triple-halogen (Cl-Br-I) fluid inclusion LA-ICP-MS microanalysis to unravel iodine behavior and sources during marine fluid infiltration into the basement in unconformity settings. Geochim. Cosmochim. Acta 357, 64–76. https://doi.org/10.1016/j.gca.2023.06.023.

Seo, J.H., Guillong, M., Aerts, M., Zajacz, Z., Heinrich, C.A., 2011. Microanalysis of S, Cl, and Br in fluid inclusions by LA–ICP-MS. Chem. Geol. 284, 35–44. https://doi.org/10.1016/j.chemgeo.2011.02.003.

Seo, J.H., Yoo, B.C., Villa, I.M., Lee, J.H., Lee, T., Kim, C., Moon, K.J., 2017. Magmatic–hydrothermal processes in Sangdong W–Mo deposit, Korea: Study of fluid inclusions and 39Ar–40Ar geochronology. Ore Geol. Rev. 91, 316–334. https://doi.org/10.1016/j.oregeorev.2017.09.019.

Sievers, N.E., Menold, C.A., Grove, M., Coble, M.A., 2017. White mica trace element and boron isotope evidence for distinctive infiltration events during exhumation of deeply subducted continental crust. Int. Geol. Rev. 59 (5–6), 621–638. https://doi.org/10.1080/00206814.2016.1219881.

Sirbescu, M.-L.C., Krukowski, E.G., Schmidt, C., Thomas, R., Samson, I.M., Bodnar, R.J., 2013. Analysis of boron in fluid inclusions by microthermometry, laser ablation ICP-MS, and Raman spectroscopy: Application to the Cryo-Genie Pegmatite, San Diego County, California, USA. Chem. Geol. 342, 138–150. https://doi.org/10.1016/j.chemgeo.2013.01.014.

Sorby, H.C., 1858. On the Microscopical, Structure of Crystals, indicating the Origin of Minerals and Rocks. Q. J. Geol. Soc. 14, 453–500. https://doi.org/10.1144/GSL.JGS.1858.014.01-02.44.

Sośnicka, M., Lüders, V., Duschl, F., Kraemer, D., Laurent, O., Niedermann, S., Banks, D. A., Wilke, F., Wohlgemuth-Ueberwasser, C., Wiedenbeck, M., 2023. Metal budget and origin of aqueous brines depositing deep-seated Zn-Pb mineralization linked to hydrocarbon reservoirs, north German Basin. Mineral. Deposita 58, 1143–1170. https://doi.org/10.1007/s00126-023-01173-z.

Steele-MacInnis, M., Bodnar, R.J., Naden, J., 2011. Numerical model to determine the composition of H2O–NaCl–CaCl2 fluid inclusions based on microthermometric and microanalytical data. Geochim. Cosmochim. Acta 75, 21–40. https://doi.org/10.1016/j.gca.2010.10.002.

Stoffell, B., Appold, M.S., Wilkinson, J.J., McClean, N.A., Jeffries, T.E., 2008. Geochemistry and evolution of Mississippi Valley-type mineralizing brines from the Tri-State and northern Arkansas districts determined by LA-ICP-MS microanalysis of fluid inclusions. Econ. Geol. 103 (7), 1411–1435.

Sun, X., Gomez-Rivas, E., Cruset, D., Alcalde, J., Muñoz-López, D., Cantarero, I., Martín-Martín, J.D., John, C.M., Travé, A., 2022. Origin and distribution of calcite cements in a folded fluvial succession: the Puig-reig anticline (South-Eastern Pyrenees). Sedimentology 69, 2319–2347. https://doi.org/10.1111/sed.12994.

Svensen, H., Jamtveit, B., Yardley, B., Engvik, A.K., Austrheim, H., Broman, C., 1999. Lead and bromine enrichment in eclogite-facies fluids: extreme fractionation during lower-crustal hydration. Geology 27 (5), 467–470.

Tang, L., Wagner, T., Fusswinkel, T., Zhang, S.-T., Hu, X.-K., Schlegel, T.U., 2021. Fluid inclusion evidence for the magmatic-hydrothermal evolution of closely linked porphyry au, porphyry Mo, and barren systems, East Qinling, China. GSA Bull. 134, 1529–1548. https://doi.org/10.1130/B36170.1.

Tannock, L., Herwegh, M., Berger, A., Liu, J., Lanari, P., Regenauer-Lieb, K., 2020. Microstructural analyses of a giant quartz reef in South China reveal episodic brittle-ductile fluid transfer. J. Struct. Geol. 130, 103911. https://doi.org/10.1016/j.jsg.2019.103911.

Tavani, S., Bertok, C., Granado, P., Piana, F., Salas, R., Vigna, B., Muñoz, J.A., 2018. The Iberia-Eurasia plate boundary east of the Pyrenees. Earth Sci. Rev. 187, 314–337. https://doi.org/10.1016/j.earscirev.2018.10.008.

Thomas, H.V., Large, R.R., Bull, S.W., Maslennikov, V., Berry, B.F., Fraser, R., Froud, S., Moye, R., 2011. Pyrite and pyrrhotite textures and composition in sediments, laminated quartz veins and reefs at Bendigo gold mine, Australia: insights for ore genesis. Econ. Geol. 106, 1–31.

Travé, A., Labaume, P., Vergés, J., 2007. Fluid Systems in Foreland Fold-and-Thrust Belts: An Overview from the Southern Pyrenees. In: Lacombe, O., Roure, F., Lavé, J., Vergés, Jaume (Eds.), Thrust Belts and Foreland Basins, Frontiers in Earth Sciences. Springer, Berlin, Heidelberg, pp. 93–115. https://doi.org/10.1007/978-3-540-69426-7_5.

Vandeginste, V., Swennen, R., Allaeys, M., Ellam, R.M., Osadetz, K., Roure, F., 2012. Challenges of structural diagenesis in foreland fold-and-thrust belts: a case study on paleofluid flow in the Canadian Rocky Mountains West of Calgary. Mar. Pet. Geol. 35, 235–251. https://doi.org/10.1016/j.marpetgeo.2012.02.014.

Vergés, J., Kullberg, J.C., Casas-Sainz, A., de Vicente, G., Duarte, L.V., Fernàndez, M., Gómez, J.J., Gómez-Pugnaire, M.T., Jabaloy Sánchez, A., López-Gómez, J., Macchiavelli, C., Martín-Algarra, A., Martín-Chivelet, J., Muñoz, J.A., Quesada, C., Terrinha, P., Torné, M., Vegas, R., 2019. An Introduction to the Alpine Cycle in Iberia. In: Quesada, C., Oliveira, J.T. (Eds.), The Geology of Iberia: A Geodynamic Approach, Regional Geology Reviews. Springer International Publishing, Cham, pp. 1–14. https://doi.org/10.1007/978-3-030-11295-0_1.

Vilà, M., Pin, C., Enrique, P., Liesa, M., 2005. Telescoping of three distinct magmatic suites in an orogenic setting: Generation of Hercynian igneous rocks of the Albera Massif (Eastern Pyrenees). Lithos 83, 97–127.

Vissers, R.L.M., van Hinsbergen, D.J.J., Wilkinson, C.M., Ganerød, M., 2017. Middle Jurassic shear zones at Cap de Creus (eastern Pyrenees, Spain): a record of pre-drift extension of the Piemonte–Ligurian Ocean? J. Geol. Soc. Lond. 174, 289–300. https://doi.org/10.1144/jgs2016-014.

Vityk, M.O., Bodnar, R.J., Doukhan, J.-C., 2000. Synthetic fluid inclusions. XV. TEM investigation of plastic flow associated with reequilibration of fluid inclusions in natural quartz. Contrib. Mineral. Petrol. 139, 285–297. https://doi.org/10.1007/s004100000142.

Wagner, T., Boyce, A.J., Erzinger, J., 2010. Fluid-rock interaction during formation of metamorphic quartz veins: a REE and stable isotope study from the Rhenish Massif, Germany. Am. J. Sci. 310, 645–682. https://doi.org/10.2475/07.2010.04.

Wagner, T., Fusswinkel, T., Wälle, M., Heinrich, C.A., 2016. Microanalysis of Fluid Inclusions in Crustal Hydrothermal Systems using Laser Ablation Methods. Elements 12, 323–328. https://doi.org/10.2113/gselements.12.5.323.

Walter, B.F., Burisch, M., Fusswinkel, T., Marks, M.A.W., Steele-MacInnis, M., Wälle, M., Apukhtina, O.B., Markl, G., 2018. Multi-reservoir fluid mixing processes in rift-related hydrothermal veins, Schwarzwald, SW-Germany. J. Geochem. Explor. 186, 158–186. https://doi.org/10.1016/j.gexplo.2017.12.004.

Warren, J.K., 1996. Evaporites, brines and base metals: what is an evaporite? Defining the rock matrix. Aust. J. Earth Sci. 43, 115–132. https://doi.org/10.1080/08120099608728241.

Wickham, S.M., Taylor, H.P., 1987. Stable isotope constraints on the origin and depth of penetration of hydrothermal fluids associated with Hercynian regional metamorphism and crustal anatexis in the Pyrenees. Contrib. Mineral. Petrol. 95, 255–268. https://doi.org/10.1007/BF00371841.

Wilkinson, J.J., 2014. 13.9 - Sediment-Hosted Zinc–Lead Mineralization: Processes and Perspectives. In: Holland, H.D., Turekian, K.K. (Eds.), Treatise on Geochemistry, Second edition. Elsevier, Oxford, pp. 219–249. https://doi.org/10.1016/B978-0-08-095975-7.01109-8.

Yang, F., Wu, G., Li, R., Zhang, T., Chen, G., Xu, Y., Li, Y., Li, T., Liu, R., Chen, Y., 2022. Age, fluid inclusion, and H–O–S–Pb isotope geochemistry of the Baiyinchagan Sn–Ag–polymetallic deposit in the southern Great Xing'an Range, NE China. Ore Geol. Rev. 150, 105194. https://doi.org/10.1016/j.oregeorev.2022.105194.

Yardley, B.W.D., 1997. The Evolution of Fluids through the Metamorphic Cycle. In: Jamtveit, B., Yardley, B.W.D. (Eds.), Fluid Flow and Transport in Rocks: Mechanisms and Effects. Springer, Netherlands, Dordrecht, pp. 99–121. https://doi.org/10.1007/978-94-009-1533-6_6.

Yardley, B.W.D., 2005. 100th anniversary special Paper: Metal Concentrations in Crustal Fluids and their Relationship to Ore Formation. Econ. Geol. 100, 613–632. https://doi.org/10.2113/gsecongeo.100.4.613.

Yardley, B.W.D., Bodnar, R.J., 2014. Fluids in the Continental Crust. Geochem. Perspect. 3, 1–2.

Yardley, B.W.D., Graham, J.T., 2002. The origins of salinity in metamorphic fluids. Geofluids 2, 249–256. https://doi.org/10.1046/j.1468-8123.2002.00042.x.